

**IRON-ADDED NICKEL COBALT SULFIDE ON NICKEL  
FOAM AS ELECTRODE FOR HIGH-PERFORMANCE  
SUPERCAPACITOR**



**A Thesis Submitted in Partial Fulfillment of the Requirements for the  
Degree of Master of Science in Chemistry  
Suranaree University of Technology  
Academic Year 2019**

ข้าวไฟฟ้านิกเกิลโคบอลต์ซัลไฟด์ที่เติมเหล็กบนแผ่นนิกเกิลโฟม  
สำหรับตัวเก็บประจุยิ่งยวดประสิทธิภาพสูง



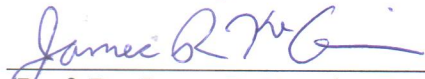
นางสาวประไพพร พรสุขสว่าง

วิทยานิพนธ์นี้เป็นส่วนหนึ่งของการศึกษาตามหลักสูตรปริญญาวิทยาศาสตรมหาบัณฑิต  
สาขาวิชาเคมี  
มหาวิทยาลัยเทคโนโลยีสุรนารี  
ปีการศึกษา 2562

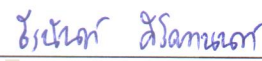
**IRON-ADDED NICKEL COBALT SULFIDE ON NICKEL FOAM  
AS ELECTRODE FOR HIGH-PERFORMANCE  
SUPERCAPACITOR**

Suranaree University of Technology has approved this thesis submitted in partial fulfillment of the requirements for a Master's degree.


Thesis Examining Committee

  
\_\_\_\_\_  
(Prof. Dr. James R. Ketudat-Cairns)

Chairperson

  
\_\_\_\_\_  
(Asst. Prof. Dr. Theeranun Siritanon)

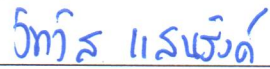
Member (Thesis Advisor)

  
\_\_\_\_\_  
(Prof. Dr. Jatuporn Wittayakun)

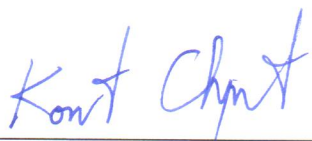
Member

  
\_\_\_\_\_  
(Assoc. Prof. Dr. Sanchai Prayoonpokarach)


Member

  
\_\_\_\_\_  
(Dr. Wittawat Saenrang)

Member

  
\_\_\_\_\_  
(Assoc. Prof. Flt. Lt. Dr. Kontorn Chamniprasart)

Vice Rector for Academic Affairs  
and Internationalization

  
\_\_\_\_\_  
(Assoc. Prof. Dr. Worawat Meevasana)

Dean of Institute of Science



PRAPHAIPHON PHONSUKSAWANG : IRON-ADDED NICKEL COBALT  
SULFIDE ON NICKEL FOAM AS ELECTRODE FOR HIGH-PERFORMANCE  
SUPERCAPACITOR. THESIS ADVISOR : ASST. PROF. THEERANUN  
SIRITANON, Ph.D. 87 PP.

SUPERCAPACITOR/NICKEL COBALT SULFIDE/BINDER-FREE

Supercapacitors are energy storage devices which are capable of fast charge-discharge. The most important component of supercapacitor is the electrode. Nickel cobalt sulfides with high electrochemical activity, high capacitance and high electrical conductivity are widely studied as electrodes for supercapacitors. The current work studies the binder-free  $\text{NiCo}_2\text{S}_4$  electrode prepared by a simple one-step hydrothermal method with the addition of  $\text{FeCl}_3$ . Effects of the amount of  $\text{Fe}^{3+}$  ion on structure, morphology and electrochemical performance are investigated. While adding  $\text{FeCl}_3$  has no effect on the crystal structure, the sample morphologies change from net-like to agglomerated 3-D particles. The specific capacitance of the prepared  $\text{NiCo}_2\text{S}_4$  electrode is 98 mAh/g at 10 A/g. The value significantly increases with added  $\text{FeCl}_3$  content and adding 1.61 mol% of  $\text{FeCl}_3$  increase the specific capacitance to 167 mAh/g at 10 A/g, which is a 170% improvement. Both experimental and computational results revealed that the enhanced performance is caused by the improved electrical conductivity and improved electrolyte adsorption. The prepared electrodes show moderate cycle stability as the capacitance is maintain at least 58% of the original value after 1,000 cycles.

School of Chemistry

Academic Year 2019

Student's Signature 

Advisor's Signature 

## ACKNOWLEDGEMENTS

I am so glad that all parts of my thesis have been achieved. As a master student, I believe I have learned a lot of things from this work. In this regard, I would like to express my sincere thanks to many people who generously helped me throughout my thesis.

Firstly, my deepest appreciation goes to my advisor, Asst. Prof. Dr. Theeranun Siritanon. Everything I have studied within this thesis has been continually supported by her. She is smart, reasonable and positive. I am so grateful for her patience to guide and encourage me along with my work.

I would like to thank the committee including Prof. Dr. James Kedudat-Cairns, Prof. Dr. Jatuporn Wittayakun, Assoc. Prof. Dr. Sanchai Prayoonpokarach and Dr. Wittawat Saenrang for their insightful comments and useful suggestions.

All experiments in this work could not have been done without the help and support from the colleagues in the Synchrotron Light Research Institute (SLRI), Dr. Narong Chanlek and Dr. Suchinda Sattayaporn, our colleague in the National Nanotechnology Center (NANOTEC), Dr. Teera Butburee, and office staff in the Center for Scientific and Technological Equipment (CSTE). Many thanks to the Center for Scientific and Technological Equipment (CSTE), Synchrotron Light Research Institute (SLRI), Meevasana group, and Advanced Materials Physics Laboratory (AMP) for providing facilities for my research.

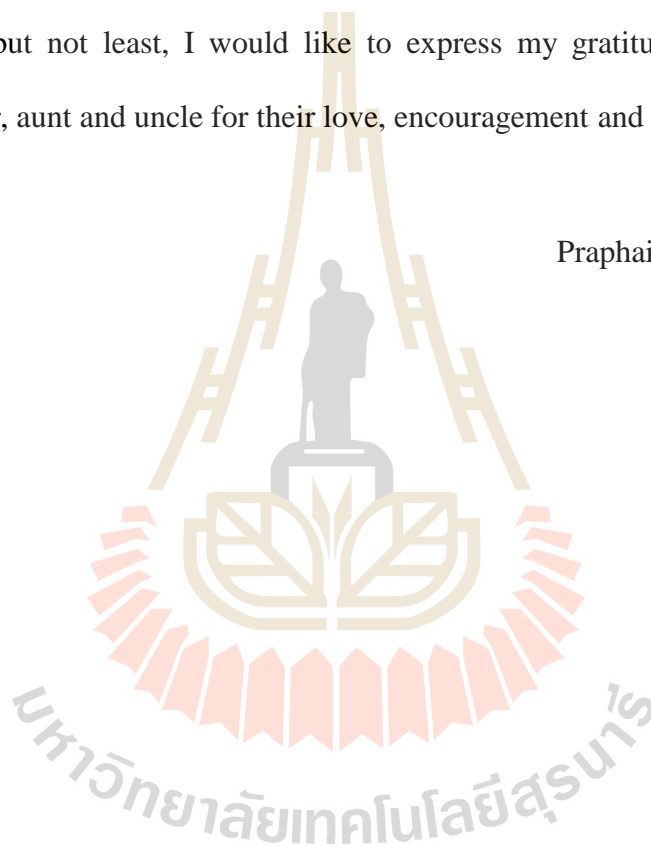
Special thanks to colleagues in computational team: Patcharaporn Khajondetchairit, Dr. Pussana Hirunsit and Dr. Suwit Suthirakun for their contribution

on calculations that completed my work. Thanks to the solid state chemistry research group, Arreerat Jiamprasertboon and Anurak Waehayee, for their assistance in XPS fitting and useful discussion. Also, thanks to Napat Ngermriang for giving me the full papers to read.

Importantly, I would like to acknowledge the Development and Promotion of Science and Technology Talent Project (DPST) for financial supports.

Last but not least, I would like to express my gratitude to my family: my mother, sister, aunt and uncle for their love, encouragement and support.

Praphaiphon Phonsuksawang



# CONTENTS

	<b>Page</b>
ABSTRACT IN THAI.....	I
ABSTRACT IN ENGLISH.....	II
ACKNOWLEDGEMENTS.....	III
CONTENTS .....	V
LIST OF TABLES.....	IX
LIST OF FIGURES .....	X
<b>CHAPTER</b>	
<b>I INTRODUCTION.....</b>	<b>1</b>
1.1 Introduction.....	1
1.2 References.....	3
<b>II LITERATURE REVIEW.....</b>	<b>7</b>
2.1 Supercapacitors within energy storage system.....	7
2.2 Charge storage mechanism in supercapacitors .....	8
2.3 Electrode materials.....	11
2.3.1 Carbon-based materials.....	11
2.3.2 Transition metal oxides.....	11
2.3.3 Polymer .....	13
2.3.4 Others (metal hydroxides, metal sulfides and composites).....	14
2.4 Nickel-cobalt compounds .....	15



## CONTENTS (Continued)

	<b>Page</b>
2.4.1 Nickel cobalt oxides.....	15
2.4.2 Nickel cobalt sulfides .....	17
2.4.3 Electrochemical performance improvement in nickel cobalt sulfides.....	20
2.5 References.....	24
<b>III EXPERIMENTAL</b> .....	<b>31</b>
3.1 Chemicals.....	31
3.2 Instruments.....	31
3.3 Sample preparation .....	32
3.4 Characterizations.....	33
3.4.1 Structure identifications .....	33
3.4.1.1 X-ray diffraction (XRD) .....	33
3.4.2 Morphology.....	33
3.4.2.1 Field emission scanning electron microscopy (FESEM)/ energy dispersive X-ray spectroscopy (EDS) .....	33
3.4.2.2 Transmission electron microscopy (TEM).....	34
3.4.3 Chemical analysis.....	35
3.4.3.1 Energy dispersive X-ray spectroscopy (EDS) .....	35
3.4.3.2 Inductively coupled plasma-optical emission spectrometry (ICP-OES) .....	35
3.4.3.3 X-ray photoelectron spectroscopy (XPS).....	35

## CONTENTS (Continued)

	<b>Page</b>
3.4.3.4 X-ray absorption near edge spectroscopy (XANES) .....	36
3.4.4 Surface area .....	37
3.4.4.1 N <sub>2</sub> adsorption-desorption .....	37
3.4.5 Electrochemical measurements .....	37
3.4.5.1 Cyclic voltammetry (CV).....	38
3.4.5.2 Galvanostatic charge-discharge (GCD) .....	39
3.4.5.3 Electrochemical impedance spectroscopy (EIS).....	40
3.4.6 Calculations.....	41
3.4.6.1 Computation details .....	41
3.5 References.....	43
<b>IV RESULTS AND DISCUSSION .....</b>	<b>45</b>
4.1 Sample preparation .....	45
4.2 Sample characterizations .....	45
4.2.1 X-ray diffraction (XRD) .....	45
4.2.2 Field emission scanning electron microscopy (FESEM).....	47
4.2.3 Transmission electron microscopy (TEM)/Energy dispersive X-ray spectroscopy (EDS) .....	50
4.2.4 Inductively coupled plasma-optical emission spectrometry (ICP-OES).....	53
4.2.5 X-ray photoelectron spectroscopy (XPS).....	54
4.2.6 X-ray absorption near edge spectroscopy (XANES) .....	58

**CONTENTS (Continued)**

	<b>Page</b>
4.2.7 N <sub>2</sub> adsorption-desorption .....	59
4.3 Electrochemical measurements.....	61
4.3.1 Cyclic voltammetry (CV).....	61
4.3.2 Galvanostatic charge-discharge (GCD) .....	66
4.3.3 Electrochemical impedance spectroscopy (EIS).....	72
4.4 Calculations.....	74
4.5 References.....	79
<b>V CONCLUSION</b> .....	<b>86</b>
<b>CURRICULUM VITAE</b> .....	<b>87</b>

## LIST OF TABLES

Table	Page
2.1 Comparison among capacitor, supercapacitor and battery .....	8
2.2 Nickel cobalt sulfides with different morphologies and their supercapacitor performance. ....	21
4.1 Binding energies and Ni <sup>2+</sup> to Ni <sup>3+</sup> ratio of NiCo <sub>2</sub> S <sub>4</sub> samples.....	55
4.2 Surface properties of NiCo <sub>2</sub> S <sub>4</sub> samples and Ni foam.....	60
4.3 NiCo <sub>2</sub> S <sub>4</sub> materials prepared by various methods and their performance.....	69

## LIST OF FIGURES

Figure	Page
2.1	Ragone plot for various energy storage devices ..... 7
2.2	Supercapacitor schematic diagram ..... 8
2.3	Basic schematics for (a) EDLC and (b) pseudocapacitor of MnO <sub>2</sub> ..... 10
2.4	Cyclic voltammograms and corresponding galvanostatic discharge curve for various types of energy-storage materials. (a, c) EDLC materials (b) surface redox materials (d, e, f) intercalation-type materials (g-i) battery-like materials ..... 10
2.5	Cyclic voltammogram of MnO <sub>2</sub> in 0.1 M K <sub>2</sub> SO <sub>4</sub> electrolyte. The upper part in red is related to the oxidation from Mn(III) to Mn(IV) and the lower part in blue refers to the reduction from Mn(IV) to Mn(III)..... 12
2.6	Conducting polymer structures (a) polyaniline (PANI) (b) polypyrrole (PPy) and (c) polythiophene (PTh)..... 13
2.7	The structure of NiCo <sub>2</sub> O <sub>4</sub> with spinel structure ..... 15
2.8	The structure of NiCo <sub>2</sub> S <sub>4</sub> with space group $Fd\bar{3}m$ ..... 17
2.9	CV curves of NiCo <sub>2</sub> S <sub>4</sub> and Ni foam at scan rate 25 mV/s..... 19
2.10	CV curves of NiCo <sub>2</sub> S <sub>4</sub> and NiCo <sub>2</sub> O <sub>4</sub> at scan rate 5 mV/s..... 19
3.1	Schematic drawing of three-electrode system with working electrode (WE), counter electrode (CE) and reference electrode (RE)..... 38

## LIST OF FIGURES (Continued)

Figure	Page
3.2	Schematic illustration of a) $\text{NiCo}_2\text{S}_4$ unit cell, b) top-view, and c) side-view of $\text{NiCo}_2\text{S}_4$ (100) surface model used in the calculations ..... 42
4.1	XRD patterns of samples on Ni foam. (a) normal scan (b) finer scan in 2 theta range 25 to $42^\circ$ ..... 46
4.2	FESEM image at low magnification (left) and high magnification (right) of (a) 0Fe-NCS (b) 0.25Fe-NCS (c) 0.5Fe-NCS (d) 1Fe-NCS (e) 1.5Fe-NCS and (f) 2Fe-NCS ..... 48
4.3	FESEM image of NaCl-added $\text{NiCo}_2\text{S}_4$ ..... 49
4.4	FESEM image of $\text{NiCo}_2\text{S}_4$ adjusted to pH 3 by HCl..... 50
4.5	TEM image of (a) 0Fe-NCS (b) 0.25Fe-NCS (c) 0.5Fe-NCS and (d) 1Fe-NCS..... 50
4.6	Close-up TEM image of (a) 0Fe-NCS (b) 0.25Fe-NCS (c) 0.5Fe-NCS and (d) 1Fe-NCS..... 51
4.7	EDS elemental mapping of 0.25Fe-NCS sample ..... 52
4.8	EDS elemental mapping of 0.5Fe-NCS sample ..... 52
4.9	EDS elemental mapping of 1Fe-NCS sample ..... 53
4.10	Ni 2p spectrum of (a) 0Fe-NCS (b) 0.25Fe-NCS (c) 0.5Fe-NCS and (d) 1Fe-NCS..... 54
4.11	Co 2p spectrum of all samples..... 56
4.12	S 2p spectrum of (a) 0Fe-NCS (b) 0.25Fe-NCS (c) 0.5Fe-NCS and (d) 1Fe-NCS..... 57

## LIST OF FIGURES (Continued)

Figure	Page
4.13 Fe K-edge XANES spectra of 0.25Fe-NCS, 0.5Fe-NCS, and 1Fe-NCS .....	58
4.14 S K-edge XANES spectra of 0Fe-NCS, 0.25Fe-NCS, 0.5Fe-NCS, and 1Fe-NCS .....	59
4.15 N <sub>2</sub> adsorption/desorption isotherm of NiCo <sub>2</sub> S <sub>4</sub> samples and Ni foam.....	60
4.16 CV curves of all samples at scan rate of 5 mV/s .....	61
4.17 CV curves of 1Fe-NCS electrode at various scan rates.....	63
4.18 (a) Capacitance versus the inverse of square root of scan rate and (b) Inverse capacitance versus the square root of scan rate .....	64
4.19 The capacitance contributed from surface ( $C_{sur}$ ) and insertion process ( $C_{diff}$ ) derived from Trasatti's method .....	65
4.20 Galvanostatic charge/discharge curves of all samples at current density of 10 A/g and the specific capacity of 0Fe-NCS, 0.25Fe-NCS, 0.5Fe-NCS and 1Fe-NCS electrodes (inset).....	66
4.21 Galvanostatic discharge curves of 1Fe-NCS electrode at various current densities .....	67
4.22 Specific capacity as a function of current density for 0Fe-NCS, 0.25Fe-NCS, 0.5Fe-NCS and 1Fe-NCS electrodes .....	68
4.23 cycle performance of all samples at current density of 10 A/g .....	71
4.24 SEM images of (a) 0Fe-NCS and (b) 1Fe-NCS before and after 1,000 cycles .....	72
4.25 EIS Nyquist plots of all samples (inset) the enlarge EIS Nyquist plots .....	73

## LIST OF FIGURES (Continued)

Figure	Page
4.26	PDOS of pristine, Fe-doped NiCo <sub>2</sub> S <sub>4</sub> bulk with doping sites at Co and Ni ..... 75
4.27	Bader charges of the two topmost layers of pristine and Fe-doped surfaces where grey, teal, dark blue, and yellow circles represent Ni at topmost layer, Ni at subsurface layer, Co, and S atoms, respectively. The light blue and orange shadow highlight the negative and positive changes of charges upon doping ..... 76
4.28	Projected density of states (PDOS) of a) pristine, b) Fe substitution at Co, c) Fe substitution at topmost-layered Ni, and d) Fe substitution at sub-layered Ni of NiCo <sub>2</sub> S <sub>4</sub> (100) surfaces. The calculated values of d-band center, E <sub>d</sub> , are indicated in the inset ..... 77
4.29	Formation of KOH electrical double layer on the Fe-doped surface at a Co site ..... 78



# CHAPTER I

## INTRODUCTION

### 1.1 Introduction

Energy is involved in all activities in our daily lives, consequently energy storage is a very crucial tool. Supercapacitors are one of the candidates for next-generation energy storage system due to their high power density during charging/discharging process and long-term stability. These excellent properties cause supercapacitors to be widely used in portable electronic devices, backup systems, and electric vehicles (Chen *et al.*, 2017).

To overcome the problem of low energy density, new electrode materials for supercapacitors are being developed (Gao and Huang, 2017). Electrode materials determine the performance of supercapacitors (Wang *et al.*, 2016). The most popular materials are carbon-based materials with high surface area, the charges are stored by electric double layer capacitor (EDLC), which is based on electrostatic accumulation. However, these materials have low specific capacitance (measured in Farad per gram of active materials). Transition metal oxides such as  $\text{MnO}_2$ ,  $\text{NiO}$ , and  $\text{Co}_3\text{O}_4$ , having electroactive species for redox reactions to store charges, are widely used as electrode materials for supercapacitors (Zhang *et al.*, 2017). Their advantages are low cost, environmental friendliness, and structural stability. However, these metal oxides suffer poor electronic conductivity which limits their performance (Lin *et al.*, 2015).

Metal sulfides are one of the interesting materials for supercapacitor electrodes. Especially, nickel cobalt sulfides ( $\text{NiCo}_2\text{S}_4$ ) are widely used in many applications including as an electrocatalyst for oxygen reduction or evolution, in anodes for lithium-ion batteries, electrodes for dye-sensitized solar cells, in electrodes for supercapacitors, and in gas sensors (Gao and Huang, 2017; Wang *et al.*, 2016; Xia *et al.*, 2015; Shimizu and Yano, 2001). The preparations of electrode materials with excellent properties have become an important key. Recently, a binder-free electrode without the polymer binder (such as polytetrafluoroethylene or polyvinylidene fluoride) that is used in conventional electrode preparation was developed to reduce internal resistance (Pu *et al.*, 2014). This can be achieved by directly growing active materials on a conductive substrate such as Ni foam, carbon fiber, and Ti foil (Chen *et al.*, 2017).

It is well known that many factors such as conductivity, surface area, and morphology affect the electrochemical performance of electrodes.  $\text{NiCo}_2\text{S}_4$  with various nanostructures and nanoarrays in 0D, 1D, 2D and 3D including hollow microspheres, nanotubes, nanosheets and flower-like structures have been reported (Gao and Huang, 2017; Zhang *et al.*, 2017; Zhu *et al.*, 2016). Interestingly, the morphologies can be tuned by adding the additives during the synthesis such as ammonium fluoride ( $\text{NH}_4\text{F}$ ) (Chen *et al.*, 2017; Lin *et al.*, 2015; Zhang *et al.*, 2017), sodium acetate (NaAc) (Liang *et al.*, 2018), polyvinylpyrrolidone (PVP) (Chen *et al.*, 2018), and sodium dodecyl surfactant (SDS) (Zhu *et al.*, 2016). These additives play a key role as protective agents and/or chelating agents to prevent agglomeration in formation process.

Not only modifying the morphology, but also doping is an effective method in improving the electrodes performance. For example, P doping improves the performance

of  $\text{NiCo}_2\text{S}_4$  (Lin *et al.*, 2018) and Fe-doped  $\text{NiCo}_2\text{O}_4$  show superior properties (Liu *et al.*, 2016; Yan *et al.*, 2017). The improved capacitance may be attributed to higher reactivity and higher conductivity after P-doping. For Fe-doping, the morphology of products greatly depends on pH level of solution, therefore Fe content also plays an important role in growth mechanism. While many researchers are focusing on preparing nanostructure and composite of  $\text{NiCo}_2\text{S}_4$  (Zhu *et al.*, 2016; Yu *et al.*, 2018; Fan *et al.*, 2017; Rong *et al.*, 2018; Nguyen *et al.*, 2015), the study on doped  $\text{NiCo}_2\text{S}_4$  are scarce. To the best of our knowledge, metal ion adding or doping in  $\text{NiCo}_2\text{S}_4$  lattice have never been reported.

Herein, this study focuses on improving the electrochemical performance of  $\text{NiCo}_2\text{S}_4$  by doping Fe. The Fe-doped  $\text{NiCo}_2\text{S}_4$  is expected to enhance the capacity of electrode materials. All samples were directly grown on Ni foam by a one-step hydrothermal method. This sample preparation is expected to change their morphology with the different amount of  $\text{FeCl}_3$  additives. The electrochemical properties were evaluated in term of capacitance value obtained from cyclic voltammetry (CV) and Galvanostatic charge-discharge (GCD) measurements. Finally, the combined experimental and computational results were used to explain the positive effects of Fe doping in the prepared  $\text{NiCo}_2\text{S}_4$  electrode.

## 1.2 References

Chen, X., Chen, D., Guo, X., Wang, R., and Zhang, H. (2017). Facile Growth of Caterpillar-like  $\text{NiCo}_2\text{S}_4$  Nanocrystal Arrays on Nickel Foam for High-

- Performance Supercapacitors. **ACS Applied Materials & Interfaces**. 9: 18774-18781.
- Chen, Y. Y., Dhaiveegan, P., Michalska, M., and Lin, Y. L. (2018). Morphology-controlled synthesis of nanosphere-like NiCo<sub>2</sub>S<sub>4</sub> as cathode materials for high-rate asymmetric supercapacitors. **Electrochimica Acta**. 274: 208-216.
- Fan, Y. M., Liu, Y., Liu, X., Liu, Y., and Fan, L. Z. (2017). Hierarchical porous NiCo<sub>2</sub>S<sub>4</sub>-rGO composites for high-performance supercapacitors. **Electrochimica Acta**. 249: 1-8.
- Gao, Y. P. and Huang, K. J. (2017). NiCo<sub>2</sub>S<sub>4</sub> Materials for supercapacitor Applications. **Chemistry – An Asian Journal**. 12: 1969-1984.
- Liang, K., He, W., Deng, X., Ma, H., and Xu, X. (2018). Controlled synthesis of NiCo<sub>2</sub>S<sub>4</sub> hollow spheres as high-performance electrode materials for supercapacitors. **Journal of Alloys and Compounds**. 735: 1395-1401.
- Lin, J., Wang, Y., Zheng, X., Liang, H., Jia, H., Qi, J., Cao, J., Tu, J., Fei, W., and Feng, J. (2018). P-doped NiCo<sub>2</sub>S<sub>4</sub> nanotubes as battery-type electrodes for high-performance asymmetric supercapacitors. **Dalton Transactions**. 47: 8771-8778.
- Lin, L., Liu, J., Liu, T., Hao, J., Ji, K., Sun, R., Zeng, W., and Wang, Z. (2015). Growth-controlled NiCo<sub>2</sub>S<sub>4</sub> nanosheet arrays with self-decorated nanoneedles for high-performance pseudocapacitors. **Journal of Materials Chemistry A**. 3: 17652-17658.
- Liu, L., Zhang, H., Fang, L., Mu, Y., and Wang, Y. (2016). Facile preparation of novel dandelion-like Fe-doped NiCo<sub>2</sub>O<sub>4</sub> microspheres@nanomeshes for excellent

- capacitive property in asymmetric supercapacitors. **Journal of Power Sources**. 327: 135-144.
- Nguyen, V. H. and Shim, J. J. (2015). In situ growth of hierarchical mesoporous NiCo<sub>2</sub>S<sub>4</sub>@MnO<sub>2</sub> arrays on nickel foam for high-performance supercapacitors. **Electrochimica Acta**. 166: 302-309.
- Pu, J., Wang, T., Wang, H., Tong, Y., Lu, C. Kong, W., and Wang, Z. (2014). Direct Growth of NiCo<sub>2</sub>S<sub>4</sub> Nanotube Arrays on Nickel Foam as High-Performance Binder-Free Electrodes for Supercapacitors. **ChemPlusChem**. 79: 577-583.
- Rong, H., Chen, T., Shi, R., Zhang, Y., and Wang, Z. (2018). Hierarchical NiCo<sub>2</sub>O<sub>4</sub>@NiCo<sub>2</sub>S<sub>4</sub> nanocomposite on Ni foam as an electrode for hybrid supercapacitors. **ACS Omega**. 3: 5634-5642.
- Shimizu, Y. and Yano, T. (2001). A Solution Route to Synthesize Nickel Thiospinels. **Chemistry Letters**. 10(10): 1028-1029.
- Wang, J. G., Jin, D., Zhou, R., Shen, C., Xie, K., and Wei, B. (2016). One-step synthesis of NiCo<sub>2</sub>S<sub>4</sub> ultrathin nanosheets on conductive substrates as advanced electrodes for high-efficient energy storage. **Journal of Power Sources**. 306: 100-106.
- Xia, C., Li, P., Gandi, A. N., Schwingschlogl, U., and Alshareef, H. N. (2015). Is NiCo<sub>2</sub>S<sub>4</sub> Really a Semiconductor?. **Chemistry of Materials**. 27: 6482-6485.
- Yan, K. L., Shang, X., Li, Z., Dong, B., Li, X., Gao, W. K., Chi, J. Q., Chai, Y. M., and Liu, C. G. (2017). Ternary mixed metal Fe-doped NiCo<sub>2</sub>O<sub>4</sub> nanowires as efficient electrocatalysts for oxygen evolution reaction. **Applied Surface Science**. 416: 371-378.

- Yu, F., Chang, Z., Yuan, X., Wang, F., Zhu, Y., Fu, L., Chen, Y., Wang, H., Wu, Y., and Li, W. (2018). Ultrathin NiCo<sub>2</sub>S<sub>4</sub>@graphene with a core-shell structure as a high performance positive electrode for hybrid supercapacitors. **Journal of Materials Chemistry A**. 6: 5856-5861.
- Zhang, Z. Huang, X., Li, H., Zhao, Y., and Ma, T. (2017). 3-D honeycomb NiCo<sub>2</sub>S<sub>4</sub> with high electrochemical performance used for supercapacitor electrodes. **Applied Surface Science**. 400: 238-244.
- Zhu, J., Tang, S., Wu, J., Shi, X., Zhu, B., and Meng, X. (2016). Wearable high-performance supercapacitors based on silver-sputtered textiles with FeCo<sub>2</sub>S<sub>4</sub>-NiCo<sub>2</sub>S<sub>4</sub> composite nanotube-built multitripod architectures as advanced flexible electrodes. **Advanced Energy Materials**. 1601234.
- Zhu, T., Zhang, G., Hu, T., He, Z., Lu, Y., Wang, G., Guo, H., Luo, J., Lin, C., and Chen, Y. (2016). Synthesis of NiCo<sub>2</sub>S<sub>4</sub>-based nanostructured electrodes supported on nickel foams with superior electrochemical performance. **Journal of Materials Science**. 51: 1903-1913.

## CHAPTER II

### LITERATURE REVIEW

#### 2.1 Supercapacitors within energy storage system

Supercapacitor or electrochemical capacitor is one of energy storage devices which bridge the gap between a capacitor and a battery as represented in a Ragone plot in Figure 2.1 Supercapacitors are not able to store charge as much as batteries but can be charged and discharged in a shorter period. Another excellent property of supercapacitors is their long cycle life. Their properties comparing with other energy storage devices are shown in Table 2.1.

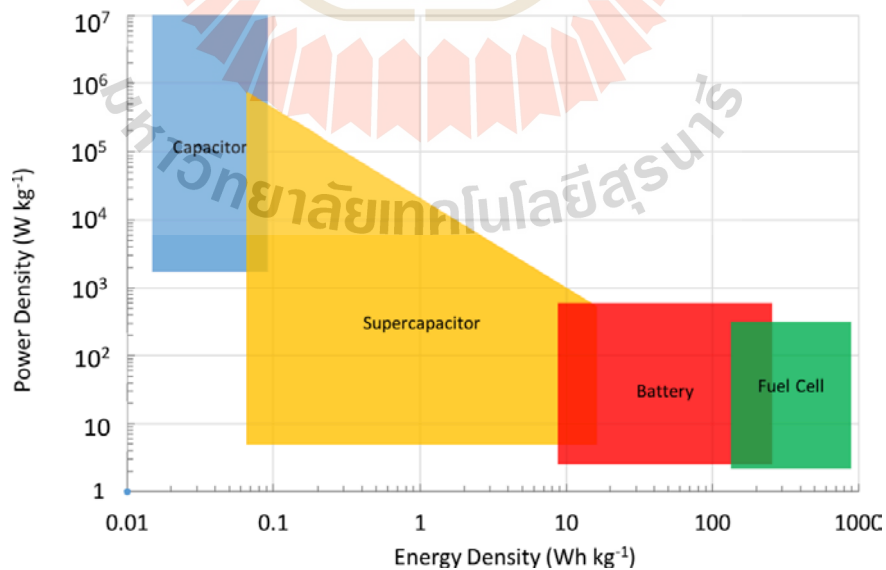


**Figure 2.1** Ragone plot for various energy storage devices (Reid, 2017).

**Table 2.1** Comparison among capacitor, supercapacitor and battery (Gonzalez *et al.*, 2016).

Characteristics	Capacitor	Supercapacitor	Battery
Specific energy (Wh/kg)	< 0.1	1-10	10-100
Specific power (W/kg)	>> 10,000	500-10,000	< 1,000
Discharge time	$10^{-6}$ to $10^{-3}$	s to min	0.3 – 3 h
Charge time	$10^{-6}$ to $10^{-3}$	s to min	1-5 h
Cycle-life	Almost infinite	> 500,000 cycles	~ 1,000 cycles

## 2.2 Charge storage mechanism in supercapacitors

A supercapacitor consists of two electrodes, an electrolyte, and a separator which isolates the two electrodes as shown in Figure 2.2. There are two charge storage mechanisms, electric double layer capacitor (EDLC) and Faradaic electron transfer.

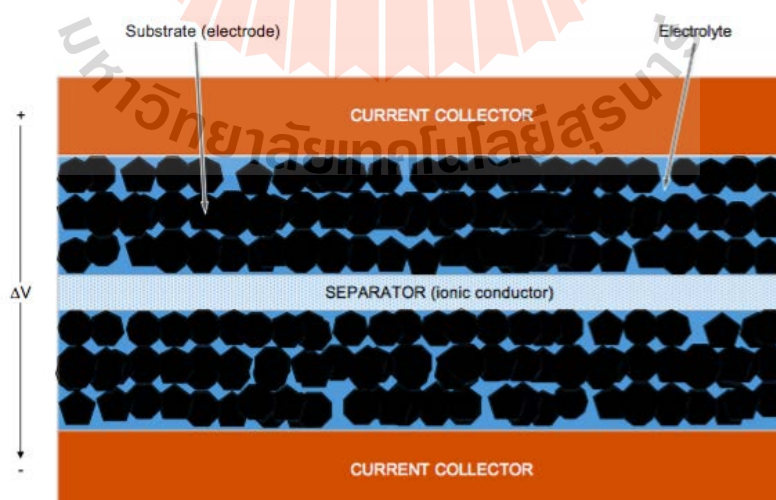


**Figure 2.2** Supercapacitor schematic diagram (Gonzalez *et al.*, 2016).



In EDLC, charges are electrostatically stored via reversible ion adsorption onto active materials (Simon and Gogotsi, 2008). This process is called non faradaic process because there is no charge transferred between the electrode and electrolyte. When voltage is applied, ions in the electrolyte diffuse to the oppositely charged electrodes. Cations and anions in the electrolyte accumulate at the electrode surface to form double layer of charge (Helmholtz layer) to avoid ion recombination (Iro *et al.*, 2016). The double layer capacitance (C) can be estimated by equation 1 as follows (Simon and Gogotsi, 2008).

$$C = \frac{\epsilon_r \epsilon_0 A}{d} \quad (1)$$

where  $\epsilon_r$  is electrolyte dielectric constant,  $\epsilon_0$  is vacuum dielectric constant, A refers to electrode surface area and d is the thickness of the double layer. Electrolyte concentration and ion size affect the double layer thickness (Kotz and Carlen, 2000).

Pseudocapacitors store charge by Faradaic reactions at the surface or near the surface of the electrodes, which involve charge transfer between the electrode and electrolyte. This process is fast and highly reversible. When voltage is applied, oxidation and reduction occur on the electrode material together with the EDLC. The capacitance of a pseudocapacitor is 10-100 times higher than that of an EDLC (Gonzalez *et al.*, 2016). Figure 2.3 shows the schematic mechanisms in an EDLC and a pseudocapacitor. Good characteristics for pseudocapacitive electrode materials are high specific capacitance and low resistance (Gonzalez *et al.*, 2016; Iro *et al.*, 2016).

In addition to Faradaic reaction at surface, batteries predominantly store charges on Faradaic electron transfer to metal center. Characteristics of batteries include having the intense and clear redox peaks in cyclic voltammograms or the plateau in charge/discharge curves (Gogotsi and Penner, 2018). The current vs. potential curves

and potential vs. time curves in Figure 2.4 provide a means to categorize the type of materials. Batteries can typically be charged/discharged in minutes to hours while charge/discharge time of EDLCs and pseudocapacitors are measured in seconds to few minutes (Gogotsi and Penner, 2018).

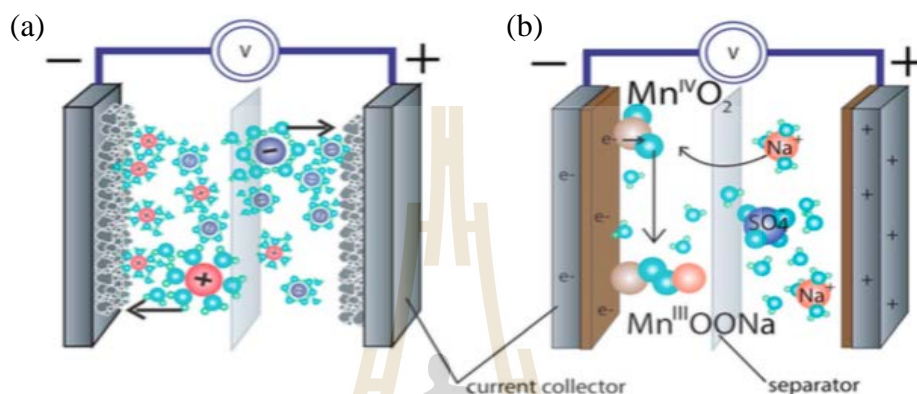


**Figure 2.3** Basic schematics for (a) EDLC and (b) pseudocapacitor of  $\text{MnO}_2$  (Jost *et al.*, 2014).

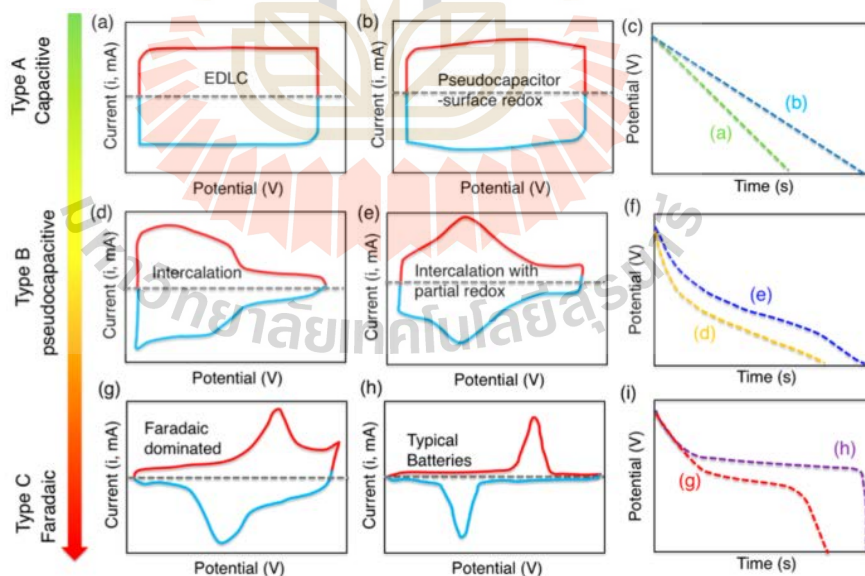


**Figure 2.4** Cyclic voltammograms and corresponding galvanostatic discharge curve for various types of energy-storage materials. (a, c) EDLC materials (b) surface redox materials (d, e, f) intercalation-type materials (g-i) battery-like materials (Gogotsi and Penner, 2018).

## 2.3 Electrode materials

Electrode material is the important part to determine the performance of supercapacitors. There are several groups of materials, including carbon-based materials, transition metal oxides, conducting polymers, sulfides, hydroxides and composites. They generally have different advantages and disadvantages.

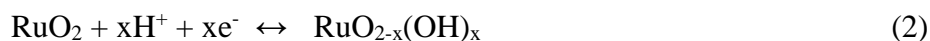
### 2.3.1 Carbon-based materials

Carbon-based materials are frequently used as electrode material in fabrication of supercapacitors due to their low cost, high availability, and high surface area especially activated carbons (AC), carbon nanotubes (CNT), and graphene (Iro *et al.*, 2016). These materials store charges by forming the electric double layer at the interface between electrode and electrolyte. The capacitance mainly depends on surface area of materials. Therefore, having high surface area with high capability for charge accumulation is required. High surface area can be achieved by physical or chemical activation. Physical activation is the treatment of carbonaceous materials at high temperature under oxidizing atmosphere ( $\text{CO}_2$  or  $\text{H}_2\text{O}$ ) while chemical activation is the treatment with chemicals such as KOH, NaOH, and  $\text{ZnCl}_2$  (Gonzalez *et al.*, 2016).

### 2.3.2 Transition metal oxides

There are many metal oxides used for supercapacitor electrodes such as  $\text{RuO}_2$ ,  $\text{MnO}_2$ , NiO, and  $\text{V}_2\text{O}_5$ . The most popular metal oxides are ruthenium and manganese oxides (Gonzalez *et al.*, 2016). Ruthenium oxides have been reported with the highest specific capacitance of  $\sim 1000$  F/g (Gonzalez *et al.*, 2016). It has three oxidation states accessible within a potential window of 1.2 V. However, it has high cost and toxicity. The pseudocapacitive behavior of  $\text{RuO}_2$  in acidic solution can be described by

equation 2 where ruthenium oxidation states change from II to IV (Gonzalez *et al.*, 2016; Simon and Gogotsi, 2008).



The value of  $x$  changes from 0 to 2 during proton insertion/de-insertion.

Less expensive oxides, such as manganese oxides, is an alternative to  $\text{RuO}_2$ . The advantages of  $\text{MnO}_2$  are low cost, low toxicity and high theoretical capacitance (1370 F/g) (Jabeen *et al.*, 2016). The charge storage mechanism is attributed to reversible redox reactions of proton incorporation as well as surface adsorption of electrolyte cations according to equation 3 (Simon and Gogotsi, 2008).



where  $\text{C}^+$  represents alkali metal cations such as  $\text{Li}^+$ ,  $\text{Na}^+$  and  $\text{K}^+$ . The oxidation states change between Mn(IV) and Mn(III) as shown in Figure 2.5.

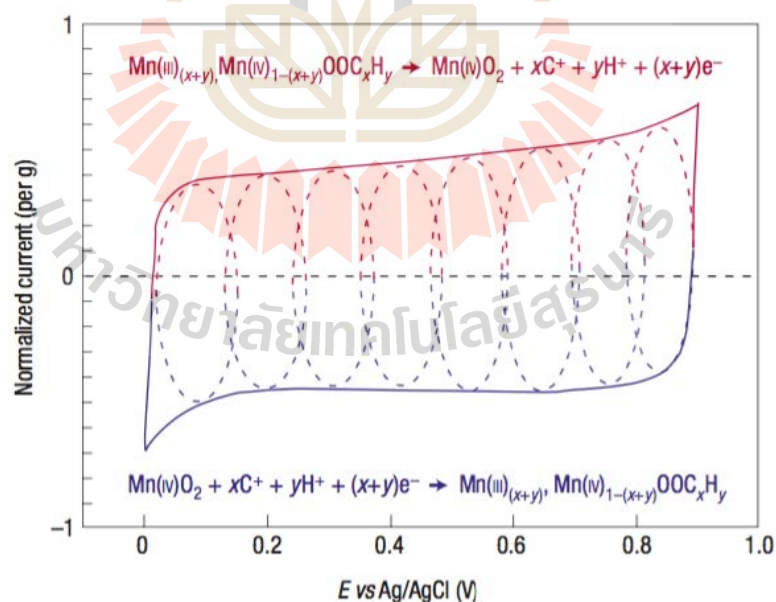


**Figure 2.5** Cyclic voltammogram of  $\text{MnO}_2$  in 0.1 M  $\text{K}_2\text{SO}_4$  electrolyte. The upper part in red is related to the oxidation from Mn(III) to Mn(IV) and the lower part in blue refers to the reduction from Mn(IV) to Mn(III) (Simon and Gogotsi, 2008).

### 2.3.3 Polymer

Conducting polymer is another type of pseudocapacitive materials used for supercapacitor electrodes. The common polymers for supercapacitor application are polypyrrole (PPy), polyaniline (PANi), and derivatives of polythiophene (PTh) (Snook *et al.*, 2011). Their structures are shown in Figure 2.6

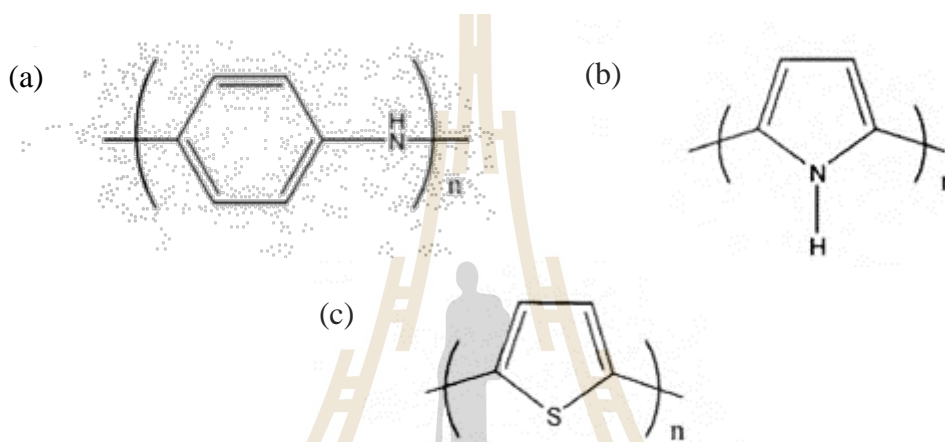
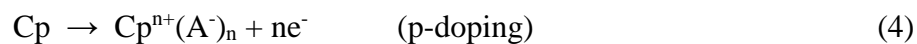


**Figure 2.6** Conducting polymer structures (a) polyaniline (PANi) (b) polypyrrole (PPy) and (c) polythiophene (PTh).

In conducting polymer (Cp), redox reaction is used to store and release charges. There are two types of conducting polymers, positively charged (p-doped) and negatively charged (n-doped). However, the lack of n-doped conducting polymer have limited their potential (Iro *et al.*, 2016). Equations 4 and 5 describe two charging processes. The discharging processes are the reverse of these equations (Snook *et al.*, 2011). When oxidation occurs (called as doping), ions are transferred to polymer backbone, when ions come back into the solution, reduction takes place (called as de-doping) (Iro *et al.*, 2016).



### 2.3.4 Others (metal hydroxides, metal sulfides and composites)

Transition metal hydroxides can be used as electrode materials for supercapacitors. The most common materials are  $\text{Co}(\text{OH})_2$  and  $\text{Ni}(\text{OH})_2$  (Shi *et al.*, 2014). They have very high theoretical specific capacitance. The calculated theoretical values of  $\text{Co}(\text{OH})_2$  and  $\text{Ni}(\text{OH})_2$  are 3460 F/g within 0.6 V and 2358 F/g within 0.44 V, respectively (Cheng *et al.*, 2014). Similar to transition metal oxides, the redox reactions occur in transition metal hydroxides during charge-discharge process. The properties of hydroxides are close to those of oxides which are poor electrical conductivity, low power density, and poor cycling stability (Shi *et al.*, 2014).

Metal sulfides, such as iron sulfides, copper sulfides, cobalt sulfides, nickel sulfides, manganese sulfides, molybdenum sulfides, and tin sulfides, have been used as electrode materials for energy storage (Rui *et al.*, 2014). These sulfides can be in different stoichiometric compositions. For example, the family of cobalt sulfides consists of  $\text{Co}_4\text{S}_3$ ,  $\text{Co}_9\text{S}_8$ ,  $\text{CoS}$ ,  $\text{Co}_3\text{S}_4$ ,  $\text{Co}_2\text{S}_3$ , and  $\text{CoS}_2$  (Rui *et al.*, 2014). From the previous reports, nickel sulfides and cobalt sulfides have excellent electrochemical performance. Therefore, they are good electrode materials for supercapacitors (Zhang *et al.*, 2017). Interestingly, ternary nickel cobalt sulfides (e.g.  $\text{NiCo}_2\text{S}_4$ ) have demonstrated better performance than binary cobalt sulfides and nickel sulfides because they can offer richer redox reactions and they have higher electrical conductivity (Wang *et al.*, 2016; Zhang *et al.*, 2017).

Another group of electrode materials is composite which combines carbon-based materials with transition metal oxides or conducting polymer. The composite electrode can store charges by both physical and chemical mechanisms (Iro *et al.*, 2016). The examples of composites are  $\text{MnO}_2/\text{CNT}$ ,  $\text{MoS}_2/\text{rGO}$  (reduced graphere oxide), and  $\text{CNT/PANi}$  (Iro *et al.*, 2016).

## 2.4 Nickel-cobalt compounds

### 2.4.1 Nickel cobalt oxides

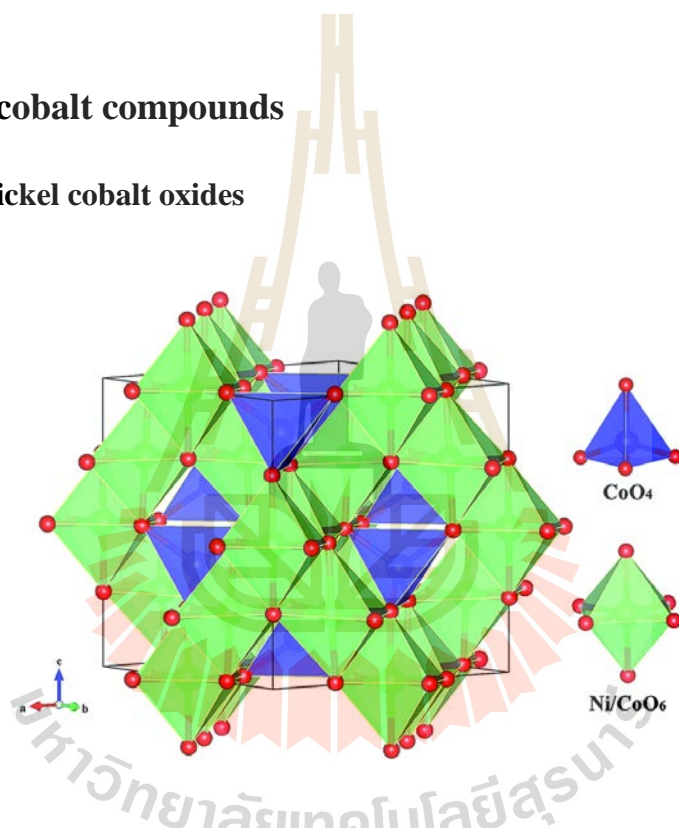
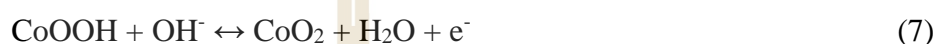
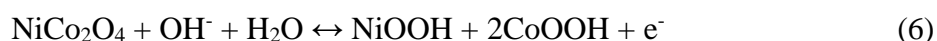


**Figure 2.7** The structure of  $\text{NiCo}_2\text{O}_4$  with spinel structure (Wu *et al.*, 2015).

Nickel cobalt oxide or nickel cobaltite ( $\text{NiCo}_2\text{O}_4$ ) has a spinel structure with general formula  $\text{AB}_2\text{O}_4$  (space group  $Fd3m$ ) as shown in Figure 2.7. Ni atoms are in the octahedron. Co atoms are located in both octahedral and tetrahedral sites. O atoms are arranged in cubic close-packed.

NiCo<sub>2</sub>O<sub>4</sub> has become a new type of electrode materials for supercapacitors. It has higher electrical conductivity and richer redox reaction than NiO and Co<sub>3</sub>O<sub>4</sub>. The sequence of electrical conductivity is as follows NiCo<sub>2</sub>O<sub>4</sub> > NiO > Co<sub>3</sub>O<sub>4</sub>. Redox reactions of NiCo<sub>2</sub>O<sub>4</sub> occur (Equations 6 and 7), with the contribution from both Ni and Co ions (Wu *et al.*, 2014).



In order to improve the properties, a few elements have been used to substitute Ni in NiCo<sub>2</sub>O<sub>4</sub>. Fujishiro *et al.* prepared 1-5 mol% Ca-doped NiCo<sub>2</sub>O<sub>4</sub> to investigate thermoelectric property at high temperature (Fujishiro *et al.*, 2004). Trivedi and Prasad studied doped spinel catalyst for oxidation of CO-CH<sub>4</sub> mixture. Pd, K, and Pd-K were doped in NiCo<sub>2</sub>O<sub>4</sub> to be used as catalyst. The performance of catalysts was improved and the activity order was as follows: K-Pd-NiCo<sub>2</sub>O<sub>4</sub> > Pd-NiCo<sub>2</sub>O<sub>4</sub> > K-NiCo<sub>2</sub>O<sub>4</sub> > NiCo<sub>2</sub>O<sub>4</sub> (Trivedi and Prasad, 2018). Liu *et al.* prepared dandelion-like Fe-doped NiCo<sub>2</sub>O<sub>4</sub> by hydrothermal method accompanied with immersion in FeCl<sub>2</sub> solution and calcination. The Fe content can be controlled by controlling the immersion time. ICP-OES results show that the Fe-content in materials increases with doping time. The NiCo<sub>2</sub>O<sub>4</sub> immersed in FeCl<sub>2</sub> solution for 1 h has specific capacitance of 2237 F/g at 1 A/g. Because this sample has unique microstructure with numerous nanoneedles on the surface and some porous nanomeshes in the inside, it exhibits large surface area and contains more active sites than pure NiCo<sub>2</sub>O<sub>4</sub> (Liu *et al.*, 2016).



### 2.4.2 Nickel cobalt sulfides

$\text{NiCo}_2\text{S}_4$  has a normal thiospinel structure of  $(\text{Ni})_A[\text{Co}_2]_B\text{S}_4$  (Figure 2.8). In this structure, Ni and Co atoms occupy one-eighth of tetrahedral sites (A) and half of octahedral sites (B), respectively (Sun *et al.*, 2017; Xia *et al.*, 2015). Comparing to oxide, the lower electronegativity of sulfur create a more flexible structure. The chemical bonds are elongated, making it easier for electron transportation (Wang *et al.*, 2016). In 1965, Bouchard *et al.* discovered the electrical conductivity of  $\text{NiCo}_2\text{S}_4$  to be  $1.25 \times 10^6$  S/m at room temperature (Bouchard *et al.*, 1965) which is about 100 times higher than that of  $\text{NiCo}_2\text{O}_4$  (Wang *et al.*, 2016; Lin *et al.*, 2015). From First-principles calculations, it was found that  $\text{NiCo}_2\text{S}_4$  show metallic conduction (Xia *et al.*, 2015).

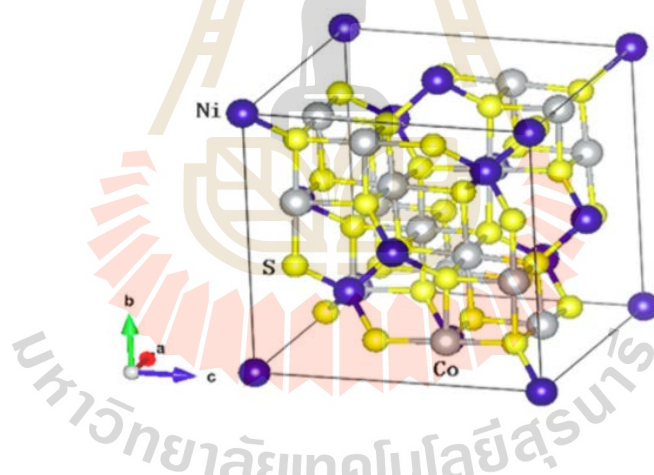


**Figure 2.8** The structure of  $\text{NiCo}_2\text{S}_4$  with space group  $Fd\bar{3}m$  (Gao and Huang, 2017).

There are three ways to prepare  $\text{NiCo}_2\text{S}_4$  materials including one-step, two-step and three-step routes (Sun *et al.*, 2017). The one-step hydrothermal method simply involves the reaction among  $\text{Ni}^{2+}$ ,  $\text{Co}^{2+}$  and sulfur source. There are also electrodeposited method reported for one-step route. Sometimes, the impurities such as  $\text{Co}_9\text{S}_8$ ,  $\text{CoS}$  and so on could occur (Gao and Huang, 2017; Sun *et al.*, 2017). Most publications on  $\text{NiCo}_2\text{S}_4$  use two-step hydrothermal preparation. First, Nickel and cobalt

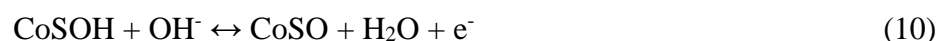
salts were transformed into  $\text{NiCo}_2(\text{OH})_{6-2x}(\text{CO}_3)_x$  ( $0 \leq x \leq 1$ ), and then converted into  $\text{NiCo}_2\text{S}_4$  by an ion-exchange reaction with  $\text{Na}_2\text{S}$ . The three-step route includes the formation of  $\text{NiCo}_2(\text{OH})_{6-2x}(\text{CO}_3)_x$  ( $0 \leq x \leq 1$ ), calcination of precursor to obtain  $\text{NiCo}_2\text{O}_4$  and finally conversion of  $\text{NiCo}_2\text{O}_4$  to  $\text{NiCo}_2\text{S}_4$  by  $\text{Na}_2\text{S}$ .

The theoretical specific capacitance of material is calculated as follows (equation 8):

$$C_s = \frac{Q}{\Delta V} = \frac{nF}{m\Delta V} \quad (8)$$

in which Q is the charge stored per gram of active material,  $\Delta V$  is the potential window (here  $\Delta V = 0.45$  V), n is the number of charges transferred during Faradaic reactions, F is Faraday constant (96485 C/mol), and m is the molar mass of active material. The calculated theoretical capacitance of  $\text{NiCo}_2\text{S}_4$  is 2111 F/g (Pu *et al.*, 2014) which is very high comparing to popular pseudocapacitive materials,  $\text{RuO}_2$  (1358 F/g) and  $\text{MnO}_2$  (1370 F/g) (Gonzalez *et al.*, 2016).

The redox peaks in CV curve of  $\text{NiCo}_2\text{S}_4$  are shown in Figure 2.9. The anodic peak at around 0.25-0.30 V and cathodic peak at around 0.10-0.15 V (Zhu *et al.*, 2015) come from reversible redox reactions of  $\text{Co}^{2+}/\text{Co}^{3+}/\text{Co}^{4+}$  and  $\text{Ni}^{2+}/\text{Ni}^{3+}$  redox couples in KOH solution as shown in Equation 9, 10, and 11 (Yang *et al.*, 2015; Gao and Huang, 2017), respectively.



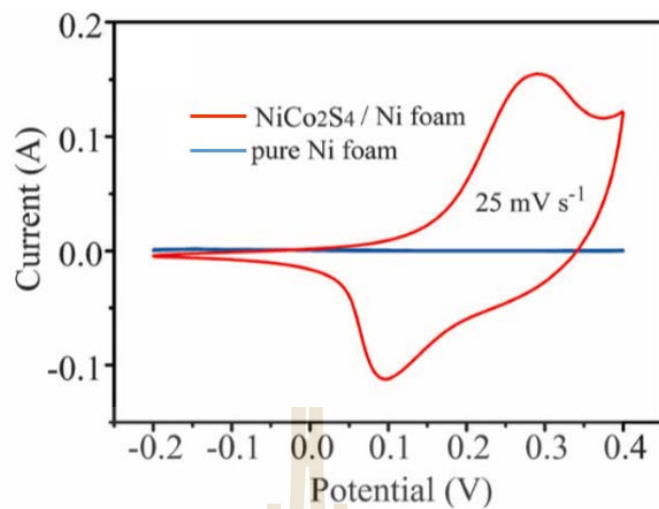


**Figure 2.9** CV curves of NiCo<sub>2</sub>S<sub>4</sub> and Ni foam at scan rate 25 mV/s (Pu *et al.*, 2014).

In Figure 2.10, the CV curve of NiCo<sub>2</sub>S<sub>4</sub> has bigger closed loop than NiCo<sub>2</sub>O<sub>4</sub> demonstrating that more charges can be stored. Therefore, nickel cobalt sulfide is a very promising candidate for supercapacitor applications.

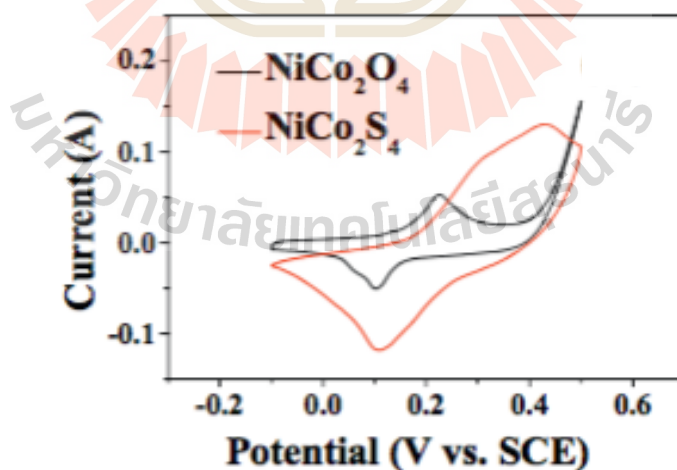


**Figure 2.10** CV curves of NiCo<sub>2</sub>S<sub>4</sub> and NiCo<sub>2</sub>O<sub>4</sub> at scan rate 5 mV/s (Yang *et al.*, 2015).

### 2.4.3 Electrochemical performance improvement in Nickel cobalt sulfides

Surface area affects the electrochemical performance because the capacitance mainly depends on surface area of materials in EDLC process. Therefore, many works focus on increasing surface area or making porous nanostructure to improve the performance (Yan *et al.*, 2018).

The morphology of this material has been widely designed in 0D, 1D, 2D and 3D nanostructures and nanoarrays (Gao and Huang, 2017). The hollow microspheres and nanoparticles are zero-dimension. These nanostructures can reduce the strain, which is good for cycling stability. The 1D nanostructures including nanorods, nanowires, and nanotubes have higher flexibility for electron transfer than 0D resulting in greater potential as electrode materials (Gao and Huang, 2017). The 2D nanostructured mainly include nanosheets and nanoflakes, which exhibit large surface area and short electron/ion pathways for transportation (Gao and Huang, 2017). The 3D structures are produced from 1D or 2D nanostructures as building blocks. For example, urchin-like structures are constructed from nanowires and nanorods (Gao and Huang, 2017) and flower-like structure are created from nanosheets (Liu and Wu, 2017; Zhang *et al.*, 2014). These 3D structures can exhibit outstanding electrochemical performance because they consist of many porous nanostructures which have large surface area (Liu and Wu, 2017).

It is well known that the morphology of materials can affect their performance as shown in Table 2.2. Zhang *et al.* reported the shape-controlled synthesis of NiCo<sub>2</sub>S<sub>4</sub>. Four morphologies including urchin-, tube-, flower- and cubic-like microstructures have been synthesized by hydrothermal with different components of mixed solvents (Zhang *et al.*, 2014). The results show that tube-like microstructures exhibit the best

performance because it has lowest charge transfer resistance ( $R_{ct}$ ), which is favorable for penetration of electrolyte ions and fast electron/ion transfer.

**Table 2.2** Nickel cobalt sulfides with different morphologies and their supercapacitor performance.

synthesis technique	morphology	specific capacitance	Ref.
hydrothermal	flaky arrays	2044 F/g at 1 A/g	Yang <i>et al.</i> , 2015
microwave-assisted	3D cauliflower-like	1471 F/g at 1 A/g	Xiao <i>et al.</i> , 2015
hydrothermal	3D petal-like	2037 F/g at 1 A/g	Wen <i>et al.</i> , 2017
template-directed method	nanocages	1635 F/g at 1 A/g	Wang <i>et al.</i> , 2016
solvothermal	hollow spheres	1036 F/g at 1 A/g	Shen <i>et al.</i> , 2015
sacrificial template method	porous nanotubes	933 F/g at 1 A/g	Wan <i>et al.</i> , 2013
hydrothermal	Hydrangea-like	1475 F/g at 3 A/g	Zhao <i>et al.</i> , 2017

Besides controlling the solvent or synthetic condition, there are a few reports on controlling the morphology of  $\text{NiCo}_2\text{S}_4$  by adding different amounts of additives. Lin *et al.* reported a synthesis of  $\text{NiCo}_2\text{S}_4$  nanoneedle arrays, nanosheet arrays and nanoneedle-decorated nanosheet arrays on Ni foam by tuning the amount of ammonium fluoride additive in two-step hydrothermal method. The  $\text{NiCo}_2\text{S}_4$  nanosheet arrays with self-decorated nanoneedles electrode show high specific capacitance of 2617.6 F/g at current density of 15 mA/cm<sup>2</sup> (Lin *et al.*, 2015). Chen *et al.* prepared 3D caterpillar-like  $\text{NiCo}_2\text{S}_4$ , composed of nanosheet core and nanowire shell grown on Ni foam by hydrothermal followed by sulfurization. Ammonium fluoride was added into the solution to obtain caterpillar-like  $\text{NiCo}_2\text{S}_4$ . They proposed the possible formation

mechanism by considering evolution process of Ni-Co precursor and tuning amount of  $\text{NH}_4\text{F}$  in the reaction. The role of  $\text{NH}_4\text{F}$  in hot solution is to make the system more acidic. Three different morphologies of  $\text{NiCo}_2\text{S}_4$  including nanosheets, nanosheets@nanoparticles and nanosheets@nanowires were obtained from different reaction time.  $\text{NiCo}_2\text{S}_4$  nanosheets@nanowires (caterpillar-like) exhibits the specific capacitance of 1777 F/g at 1 A/g. (Chen *et al.*, 2017). Zhang *et al.* synthesized 3-D honeycomb  $\text{NiCo}_2\text{S}_4$  with highly porous structure by modified hydrothermal method assisted with sulfuration. It was found that  $\text{NH}_4\text{F}$  plays important roles on morphologies. They prepared needle-, flake- and petal-like nanostructured  $\text{NiCo}_2\text{S}_4$  by adding different amounts of  $\text{NH}_4\text{F}$  to investigate the effect of morphology on electrochemical performance (Zhang *et al.*, 2017).

Not only  $\text{NH}_4\text{F}$  additive, but also other compounds such as sodium acetate (NaAc) (Liang *et al.*, 2018), polyvinylpyrrolidone (PVP) (Chen *et al.*, 2018), and sodium dodecyl surfactant (SDS) (Zhu *et al.*, 2016) were added to tune  $\text{NiCo}_2\text{S}_4$  morphologies. Liang and co-worker synthesized  $\text{NiCo}_2\text{S}_4$  with different morphologies including particles, sheets and hollow spheres. They found that the addition of NaAc transformed the morphologies from particles and nanosheets to hollow spheres. In hollow structure, the electrolyte ions can diffuse into active materials easily (Liang *et al.*, 2018). Chen *et al.* prepared nanosphere-like  $\text{NiCo}_2\text{S}_4$  by one-pot PVP-assisted hydrothermal method. The results show that the morphology change from irregular shape to nanosphere-like and the particle size is reduced by increasing the PVP concentration in solution (Chen *et al.*, 2018). Zhu *et al.* reported the synthesis of  $\text{NiCo}_2\text{S}_4$  on nickel foam via two-step hydrothermal method with addition of sodium dodecyl surfactant (SDS). The results show that the surfactant influences the crystal structure, morphology, and

electrochemical performance. NiCo<sub>2</sub>S<sub>4</sub>-pure and NiCo<sub>2</sub>S<sub>4</sub>-SDS have different crystallite size and morphology. The morphology of NiCo<sub>2</sub>S<sub>4</sub>-pure precursor showsglomerated nanoneedles leading to nanotube arrays product. On the other hand, NiCo<sub>2</sub>S<sub>4</sub>-SDS precursor have self-organized nanoneedles forming hierarchical porous structure. SDS acts as anionic surfactant to protect the agglomeration of nanoparticles. NiCo<sub>2</sub>S<sub>4</sub>-pure with finer crystallinity can increase the accessibility of electrolyte for redox reaction. In NiCo<sub>2</sub>S<sub>4</sub>-SDS, the porous structure acts as ion-buffering reservoir providing electrolyte ions for redox reactions (Zhu *et al.*, 2016).

In addition to morphological control, the defect engineering either by introducing anion vacancies or doping with other metal is one of effective strategies to improve the electrochemical performance. Oxygen vacancies in NiCo<sub>2</sub>O<sub>4</sub> have been reported not only to enhance the conductivity but also increase the capacitance by improving the adsorption of OH<sup>-</sup> for redox reaction on the surface (Yan *et al.*, 2018; Li *et al.*, 2015). Lu and co-workers found that the sulfur vacancies in NiCo<sub>2</sub>S<sub>4</sub> can enhance the capacitance by improving the electrical conductivity, but the cycle stability is lowered because of the disordering in crystal structure (Lu *et al.*, 2016). Lin *et al.* found that phosphorous-doped (P-doped) NiCo<sub>2</sub>S<sub>4</sub> showed 60% improvement in specific capacitance compared to that of the pristine NiCo<sub>2</sub>S<sub>4</sub> which attributed to the higher reactivity and conductivity after P-doping (Lin *et al.*, 2018). Similarly, iron-doping significantly improves both conductivity and specific capacitance of NiCo<sub>2</sub>O<sub>4</sub> electrodes (Liu *et al.*, 2016; Yan *et al.*, 2017). Very recently, Lai and co-worker reported that Fe doping in NiCo<sub>2</sub>S<sub>4</sub> could enhance the charge storage performance of material in ionic liquid-based supercapacitors. Based on theoretical studies by density function theory (DFT) calculations, 5 mol% Fe doping results in enhanced density of states (DOS) near

the Fermi level, indicating that the electrical conductivity is increased. After replacing Ni and Co by the less electronegative Fe atoms, the electron density is partially delocalized especially from Fe and closer to the S atoms than pristine NiCo<sub>2</sub>S<sub>4</sub>. Moreover, the ionic liquid adsorption energy of Fe-doped NiCo<sub>2</sub>S<sub>4</sub> (-4.0 eV) is lower than NiCo<sub>2</sub>S<sub>4</sub> (-3.78 eV). Thus, Fe doping can provide stronger binding sites for ionic liquid ions, EMIM<sup>+</sup> ions, leading to enhanced energy storage capacity. (Lai *et al.*, 2019).

## 2.5 References

- Bouchard, R. J., Russo, P. A., and Wold, A. (1965). Preparation and Electrical Properties of Some Thiospinels. **Inorganic Chemistry**. 4: 685-688.
- Chen, X., Chen, D., Guo, X., Wang, R., and Zhang, H. (2017) Facile Growth of Caterpillar-like NiCo<sub>2</sub>S<sub>4</sub> Nanocrystal Arrays on Nickel Foam for High-Performance Supercapacitors. **ACS Applied Materials & Interfaces**. 9(22): 18774–18781.
- Chen, Y. Y., Dhaiveegan, P., Michalska, M., and Lin, Y. L. (2018). Morphology-controlled synthesis of nanosphere-like NiCo<sub>2</sub>S<sub>4</sub> as cathode materials for high-rate asymmetric supercapacitors. **Electrochimica Acta**. 274: 208-216.
- Cheng, J. P., Zhang, J., and Liu, F. (2014). Recent development of metal hydroxides as electrode material of electrochemical capacitors. **RSC Advances**. 4: 38893-38917.
- Fujishiro, Y., Hamamoto, K., Shiono, O., Katayama, S., and Awano, M. (2004). Synthesis and thermoelectric characterization of polycrystalline Ni<sub>1-x</sub>Ca<sub>x</sub>Co<sub>2</sub>O<sub>4</sub> (x = 0-0.05) spinel materials. **Journal of Materials Science: Materials in Electronics**. 15: 769-773.



- Gao, Y. P. and Huang, K. J. (2017). NiCo<sub>2</sub>S<sub>4</sub> Materials for supercapacitor Applications. **Chemistry – An Asian Journal**. 12: 1969-1984.
- Gogotsi, Y. and Penner, R. M. (2018). Energy Storage in Nanomaterials – Capacitive, Pseudocapacitive, or Battery-like. **ACS Nano**. 12: 2081-2083.
- Gonzalez, A., Goikorea, E., Barrena, J. A., and Mysyk, R. (2016). Review on supercapacitors: Technologies and materials. **Renewable and Sustainable Energy Reviews**. 58: 1189-1206.
- Iro, Z. S., Subramani, C., and Dash, S. S. (2016). A Brief Review on Electrode Materials for Supercapacitor. **International Journal of Electrochemical Science**. 11: 10628-10643.
- Jabeen, N., Xia, Q., Savilov, S. V., Aldoshin, S. M., Yu, Y., and Xia, H. (2016) Enhanced Pseudocapacitive Performance of  $\alpha$ -MnO<sub>2</sub> by Cation Preinsertion. **ACS Applied Materials & Interfaces**. 8(49): 33732-33740.
- Jost, K., Dion, G., and Gogotsi, Y. (2014). Textile energy storage in perspective. **Journal of Materials Chemistry A**. 2: 10776-10787.
- Kotz, R. and Carlen, M. (2000). Principles and applications of electrochemical capacitors. **Electrochimica Acta**. 45: 2483-2498.
- Lai, F., Feng, J., Heil, T., Tian, Z., Schmidt, J., Wang, G. C., and Oschatz, M. (2019) Partially delocalized charge in Fe-doped NiCo<sub>2</sub>S<sub>4</sub> nanosheet- mesoporous carbon-composites for high-voltage supercapacitors. **Journal of Materials Chemistry A**. 7: 19342-19347.
- Li, X., Jiang, L., Zhou, C., Liu, J., and Zeng, H. (2015). Integrating large specific surface area and high conductivity in hydrogenated NiCo<sub>2</sub>O<sub>4</sub> double-shell hollow spheres to improve supercapacitors. **NPG Asia Materials**. 7: 1-7.

- Liang, K., He, W., Deng, X., Ma, H., and Xu, X. (2018). Controlled synthesis of NiCo<sub>2</sub>S<sub>4</sub> hollow spheres as high-performance electrode materials for supercapacitors. **Journal of Alloys and Compounds**. 735: 1395-1401.
- Lin, J., Wang, Y., Zheng, X., Liang, H., Jia, H., Qi, J., Cao, J., Tu, J., Fei, W., and Feng, J. (2018). P-Doped NiCo<sub>2</sub>S<sub>4</sub> nanotubes as battery-type electrodes for high-performance asymmetric supercapacitors. **Dalton Transactions**. 47: 8771-8778.
- Lin, L., Liu, J., Liu, T., Hao, J., Ji, K., Sun, R., Zeng, W., and Wang, Z. (2015). Growth-controlled NiCo<sub>2</sub>S<sub>4</sub> nanosheet arrays with self-decorated nanoneedles for high-performance pseudocapacitors. **Journal of Materials Chemistry A**. 3: 17652-17658.
- Liu, L., Zhang, H., Fang, L., Mu, Y., and Wang, Y. (2016). Facile preparation of novel dandelion-like Fe-doped NiCo<sub>2</sub>O<sub>4</sub> microspheres@nanomeshes for excellent capacitive property in asymmetric supercapacitors. **Journal of Power Sources**. 327: 135-144.
- Liu, X. and Wu, Z. (2017). Hierarchitectures of mesoporous flowerlike NiCo<sub>2</sub>S<sub>4</sub> with excellent pseudocapacitive properties. **Materials Letters**. 187: 24-27.
- Lu, F., Zhou, M., Li, W., Weng, Q., Li, C., Xue, Y., Jiang, X., Zeng, X., Bando, Y., and Golberg, D. (2016). Engineering sulfur vacancies and impurities in NiCo<sub>2</sub>S<sub>4</sub> nanostructures toward optimal supercapacitive performance. **Nano Energy**. 26: 313-323.
- Pu, J., Wang, T., Wang, H., Tong, Y., Lu, C. Kong, W., and Wang, Z. (2014). Direct Growth of NiCo<sub>2</sub>S<sub>4</sub> Nanotube Arrays on Nickel Foam as High-Performance Binder-Free Electrodes for Supercapacitors. **ChemPlusChem**. 79: 577-583.

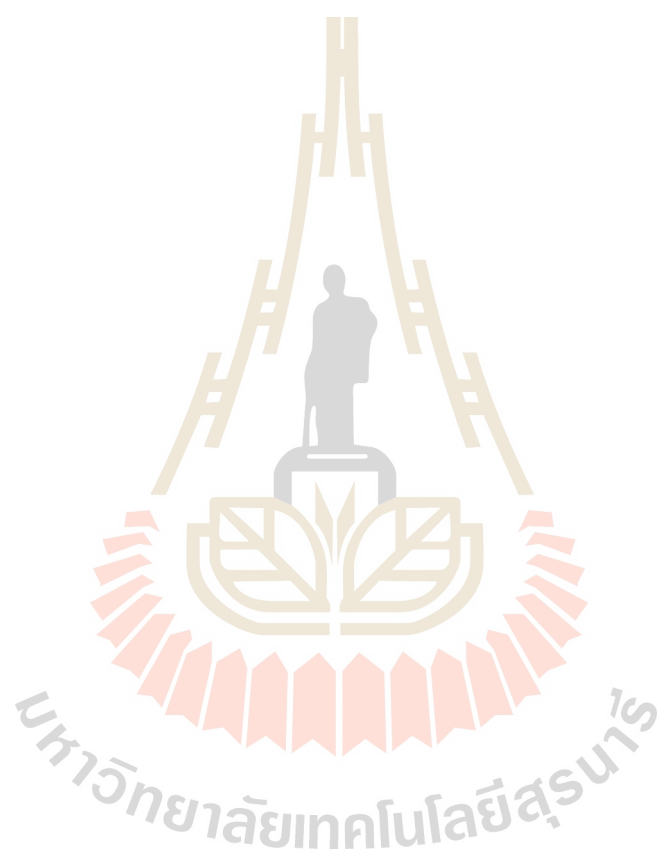
- Reid, D. O. (2017). Advanced Fibre Based Energy Storage. University of Surrey (United Kingdom).
- Rui, X., Tan, H., and Yan, Q. (2014). Nanostructured metal sulfides for energy storage. **Nanoscale**. 6: 9889-9924.
- Shen, L., Yu, L., Wu, H. B., Yu, X. Y., Zhang, X., and Lou, X. W. (2015). Formation of nickel cobalt sulfide ball-in-ball hollow spheres with enhanced electrochemical pseudocapacitive properties. **Nature Communications**. 6: 6694-6701.
- Shi, F., Wang, X. L., Gu, C. D., and Tu, J. P. (2014). Metal oxide/hydroxide-based materials for supercapacitors. **RSC Advances**. 4: 41910-41921.
- Shown, I., Ganguly, A., Chen, L. C., and Chen, K. H. (2015). Conducting polymer-based flexible supercapacitor. **Energy Science and Engineering**. 3(1): 2-26.
- Simon, P. and Gogotsi, Y. (2008). Materials for electrochemical capacitors. **Nature materials**. 7: 845-854.
- Snook, G. A., Kao, P., and Best A. S. (2011). Conducting-polymer-based supercapacitor devices and electrodes. **Journal of Power Sources**. 196: 1-12.
- Sun, M., Tie, J., Li, Y., and Yu, L. (2017). NiCo<sub>2</sub>S<sub>4</sub>-Based Materials for Electrochemical Applications. **General Chemistry**. 3: 202-206.
- Trivedi, S. and Prasad, R. (2018). Synthesis of K-Pd doped NiCo<sub>2</sub>O<sub>4-δ</sub> by reactive calcination route for oxidation of CO-CH<sub>4</sub> emissions from CNG vehicles. **New Journal of Chemistry**. 42: 4142-4154.
- Wan, H. Z., Jiang, J., Yu, J., Xu, K., Miao, L., Zhang, L., Chen, H., and Ruan, Y. (2013). NiCo<sub>2</sub>S<sub>4</sub> porous nanotubes synthesis via sacrificial templates: high-

- performance electrode materials of supercapacitors. **CrystEngComm**. 15: 7649-7651.
- Wang, J. G., Jin, D., Zhou, R., Shen, C., Xie, K., and Wei, B. (2016). One-step synthesis of NiCo<sub>2</sub>S<sub>4</sub> ultrathin nanosheets on conductive substrates as advanced electrodes for high-efficient energy storage. **Journal of Power Sources**. 306: 100-106.
- Wang, J. G., Zhou, R., Jin, D., Xie, K., and Wei, B. (2016). Controlled synthesis of NiCo<sub>2</sub>S<sub>4</sub> nanostructures on nickel foams for high-performance supercapacitors. **Energy Storage Materials**. 2: 1-7.
- Wang, Z., He, B., Kong, W., and Lu, C. (2016). Synthesis of NiCo<sub>2</sub>S<sub>4</sub> Nanocages as Pseudocapacitor Electrode Materials. **ChemistrySelect**. 1: 4082-4086.
- Wen, Y., Peng, Y., Wang, Z., Hao, J., Qin, T., Lu, S., Zhang, J., He, D., Fan, X., and Cao, G. (2017). Facile synthesis of ultrathin NiCo<sub>2</sub>S<sub>4</sub> nano-petals inspired by blooming buds for high-performance supercapacitors. **Journal of Materials Chemistry A**. 5: 7144-7152.
- Wu, J., Guo, P., Liu, X., Zhang, H., Mei, J., Liu, H., Lau, W. M., and Liu, L. M. (2015). Ultrathin NiCo<sub>2</sub>O<sub>4</sub> nanosheets grown on three-dimensional interwoven nitrogen-doped carbon nanotubes as binder-free electrodes for high-performance supercapacitor. **Journal of Material Chemistry A**. 3: 15331-15338.
- Wu, Z., Zhu, Y., and Ji, X. (2014). NiCo<sub>2</sub>O<sub>4</sub>-based materials for electrochemical supercapacitors. **Journal of Materials Chemistry A**. 2: 14759-14772.
- Xia, C., Li, P., Gandi, A. N., Schwingenschlogl, U., and Alshareef, H. N. (2015). Is NiCo<sub>2</sub>S<sub>4</sub> Really a Semiconductor?. **Chemistry of Materials**. 27: 6482-6485.

- Xiao, Y., Lei, Y., Zheng, B., Gu, L., Wang, Y., and Xiao, D. (2015). Rapid microwave-assisted fabrication of 3D cauliflower-like  $\text{NiCo}_2\text{S}_4$  architectures for asymmetric supercapacitors. **RSC Advances**. 5: 21604-21613.
- Yan, K. L., Shang, X., Li, Z., Dong, B., Li, X., Gao, W. K., Chi, J. Q., Chai, Y. M., and Liu, C. G. (2017). Ternary mixed metal Fe-doped  $\text{NiCo}_2\text{O}_4$  nanowires as efficient electrocatalysts for oxygen evolution reaction. **Applied Surface Science**. 416: 371-378.
- Yan, D., Wang, W., Luo, X., Chen, C., Zeng, Y., and Zhu, Z. (2018).  $\text{NiCo}_2\text{O}_4$  with oxygen vacancies as better performance electrode material for supercapacitor. **Chemical Engineering**. 334: 864-872.
- Yang, Z., Zhu, X., Wang, K., Ma, G., Cheng, H., and Xu, F. (2015). Preparation of  $\text{NiCo}_2\text{S}_4$  flaky arrays on Ni foam as binder-free supercapacitor electrode. **Applied Surface Science**. 347: 690-695.
- Zhang, Y., Ma, M., Yang, J., Sun, C., Su, H., Huang, W., and Dong, X. (2014). Shape-controlled synthesis of  $\text{NiCo}_2\text{S}_4$  and their charge storage characteristics in supercapacitors. **Nanoscale**. 6: 9824-9830.
- Zhang, Z. Huang, X., Li, H., Zhao, Y., and Ma, T. (2017). 3-D honeycomb  $\text{NiCo}_2\text{S}_4$  with high electrochemical performance used for supercapacitor electrodes. **Applied Surface Science**. 400: 238-244.
- Zhao, F. L., Huang, W. X., Shi, Q., Zhou, D., Zhao, L., and Zhang, H. (2017). Low temperature fabrication of hydrangea-like  $\text{NiCo}_2\text{S}_4$  as electrode materials for high performance supercapacitors. **Materials Letters**. 186: 206-209.
- Zhu, T., Zhang, G., Hu, T., He, Z., Lu, Y., Wang, G., Guo, H., Luo, J., Lin, C., and Chen, Y. (2016). Synthesis of  $\text{NiCo}_2\text{S}_4$ -based nanostructured electrodes

supported on nickel foams with superior electrochemical performance.

**Journal of Materials Science.** 51: 1903-1913.



# CHAPTER III

## EXPERIMENTAL

### 3.1 Chemicals

- Nickel(II) nitrate hexahydrate ( $\text{Ni}(\text{NO}_3)_2 \cdot 6\text{H}_2\text{O}$ ), 99%, Acros Organics
- Cobalt(II) nitrate hexahydrate ( $\text{Co}(\text{NO}_3)_2 \cdot 6\text{H}_2\text{O}$ ), 99+%, Acros Organics
- Thiourea ( $\text{CS}(\text{NH}_2)_2$ ), 99+%, Carlo Erba
- Anhydrous iron(III) chloride ( $\text{FeCl}_3$ ), Carlo Erba
- Ethylene glycol ( $(\text{CH}_2\text{OH})_2$ ), Carlo Erba
- Potassium hydroxide (KOH), Carlo Erba

### 3.2 Instruments

- Powder X-ray diffractometer (XRD), Model D2 Phaser, Bruker
- Field emission scanning electron microscope (FESEM)/Energy dispersive X-ray spectroscopy (EDS), Zeiss AURIGA
- Transmission electron microscope (TEM), JEOL2100plus
- X-ray photoelectron spectroscopy (XPS), PHI5000 VersaProbe II XPS instruments (ULVAC-PHI, Japan)
- X-ray absorption near edge spectroscopy (XANES), SUT-NANOTEC-SLRI beamline5.2, Synchrotron light research institute
- Inductively coupled plasma-optical emission spectrometry (ICP-OES), PerkinElmer Optima 8300
- $\text{N}_2$  adsorption-desorption, Bel-Japan Bel Sorp mini II

### 3.3 Sample preparation

All samples were prepared by a simple one-step hydrothermal method. The Ni foam (1 cm x 2 cm, with 0.08 mm thickness) was used as a conductive substrate. In a synthesis of  $\text{NiCo}_2\text{S}_4$ , 0.5 mmol of  $\text{Ni}(\text{NO}_3)_2 \cdot 6\text{H}_2\text{O}$ , 1 mmol of  $\text{Co}(\text{NO}_3)_2 \cdot 6\text{H}_2\text{O}$ , and 2 mmol of thiourea were dissolved in 20 mL of deionized water/ethylene glycol mixture (1:1 by volume) under magnetic stirring for 30 min. The mixed homogeneous solution was transferred to a Teflon-lined stainless steel autoclave with a piece of Ni foam immersed in the solution. The autoclave was put in an oven and heated at 90 °C for 8 h. After it was naturally cooled down to room temperature, the dark black product (designated as 0Fe-NCS) was obtained on Ni foam, which was washed with deionized water for several times. A series of samples were synthesized under the same condition, but with different amounts of  $\text{FeCl}_3$  addition. Six samples of Fe-added  $\text{NiCo}_2\text{S}_4$  were prepared by adding 0.12 mmol (assigned as 0.25Fe-NCS following the mole ratio of Fe:Ni), 0.25 mmol (0.5Fe-NCS), 0.5 mmol (1Fe-NCS), 0.75 mmol (1.5Fe-NCS) and 1 mmol (2Fe-NCS) of  $\text{FeCl}_3$ . The mass loading of all samples was calculated by the weight difference of Ni foam before and after the reaction.



## **3.4 Characterizations**

### **3.4.1 Structure identifications**

#### **3.4.1.1 X-ray diffraction (XRD)**

X-ray diffraction is a nondestructive technique, widely used for phase identification and crystal structure determination. The monochromatic X-ray interacts with matter by scattering. According to Bragg's law ( $n\lambda = 2d\sin\theta$ ), the constructive interferences occur when the scattered X-rays are coherent and these contribute to X-ray diffraction patterns. The X-ray diffraction patterns are used as fingerprints to identify the crystal phase in the sample.

In this study, the obtained products on Ni foam were put on the silica sample holder. The XRD spectra were carried out at room temperature using a D2 Phaser XRD diffractometer (Bruker) with Cu K $\alpha$  radiation ( $\lambda = 1.5406 \text{ \AA}$ ) operating at the voltage of 30 kV and the current of 10 mA. The XRD patterns were collected in 2theta range of 10-60° with an increment of 0.02° at a scan rate of 0.2s/step. We also collected the XRD patterns with finer step and longer time at a scan rate of 2s/step in 2theta range of 25-42°. The phase identification and the crystal structure were identified with databases by using DIFFRACT.EVA software.

### **3.4.2 Morphology**

#### **3.4.2.1 Field emission scanning electron microscopy (FESEM)/**

#### **Energy dispersive X-ray spectroscopy (EDS)**

This electron microscope provides the information about surface topography of the sample. Compared with typical SEM, field emission SEM produces the high-quality images with high resolution. The brighter and smaller electron beam

from field emission source strikes the atoms within the sample, the various signals are generated. There are three signals including secondary electrons, backscattered electrons and X-ray. The detector catches the secondary electrons and transforms to the image of sample's surface topography.

In the experiments, the samples were prepared on a layer of carbon without gold coating because of its conductive nature. The SEM images were taken by a Zeiss AURIGA FE-SEM with high magnification. Energy dispersive X-ray spectroscopy (EDS) and elemental mapping were used for area analysis. These techniques reveal the information about morphology, particle size, elemental composition and their distribution in the samples.

#### **3.4.2.2 Transmission electron microscopy (TEM)**

TEM operates on the same principle as light microscope but using electron instead of light. The high energy beam of electron from an electron gun is transmitted through very thin sample on a grid. The portion of transmitted beam is magnified and focused by objective lens into an image on viewing screen such as charge coupled device (CCD) camera. The darker areas in the images indicate that fewer electrons are transmitted through those area of sample. On the other hand, the lighter areas indicate that more electrons are passing that area. Therefore, TEM provides the details about morphology of the sample. Additionally, as the electrons pass through the specimen, they are scattered by elements in the sample to generate diffraction pattern. This pattern reveals the information about the crystallinity of materials.

In this work, each electrode was immersed in ethanol and sonicated for several hours to disperse NiCo<sub>2</sub>S<sub>4</sub> phase in ethanol which was later dropped onto the Cu grid and dried at room temperature for TEM analysis.

### **3.4.3 Chemical analysis**

#### **3.4.3.1 Energy dispersive X-ray spectroscopy (EDS)**

By electron bombardment, the core electrons are ejected out of an atom and leave the holes. An outer-shell electron fills a hole and releases the X-ray energy. This characteristic X-ray emission can be used to identify the elements and their proportion in the sample.

By using EDS connected to SEM or TEM, the elemental mapping analysis were carried out in the interested area of the image to quantitatively analyze each element and their distribution in the sample.

#### **3.4.3.2 Inductively coupled plasma-optical emission spectrometry (ICP-OES)**

ICP-OES is an analytical technique used to detect the chemical composition in the sample. The excited atoms are produced by extremely hot plasma. When electrons return to ground state, they emit electromagnetic radiation at particular wavelength. Each element has its own characteristic emission spectrum. The content of each element within the sample is then determined based on the intensity of the emission.

It should be noted that, the samples on Ni foam were digested with acid solution of  $\text{HNO}_3$  and  $\text{H}_2\text{O}_2$  prior to ICP-OES analysis.

#### **3.4.3.3 X-ray photoelectron spectroscopy (XPS)**

XPS is the surface-sensitive technique used for determination of chemical state and elemental composition. When X-ray interact with atoms from the top 1-10 nm of material, the photoelectron are ejected due to photoelectric effect. The kinetic energy

of emitted photoelectron is measured and used to calculate the binding energy of electrons. The binding energy is characteristic of a particular element.

In this study, XPS spectra were collected by a PHI5000 VersaProbe II XPS instruments (ULVAC-PHI, Japan) with monochromatic X-ray of Al K $\alpha$  (1486.6 eV). The binding energies were calibrated with C1s peak at 284.8 eV. The XPS spectra were fitted by the Gaussian method using CasaXPS software.

#### **3.4.3.4 X-ray absorption near edge spectroscopy (XANES)**

This absorption technique is a synchrotron-based technique which provides intense and tunable X-ray beams. To obtain the XANES spectra, the photon energy is tuned in the range covering the absorption edge, 10 eV below the absorption edge and 20 eV above, where the core electrons can be excited. The excitation of a 1s electron occurs at K-edge. The fundamental processes in XANES are photoabsorption of X-ray into a core level followed by photoelectron emission and filling of the core hole by an electron in another level, resulting in emission of either fluorescence or an Auger electron.

In this work, the oxidation states of Fe and S were determined by XANES. Fe K-edge and S K-edge measurements were carried out in fluorescence mode at the SUT-NANOTECH-SLRI beamline5.2, Synchrotron Light Research Institute, Nakhon Ratchasima, Thailand. The XANES data was processed by Athena program.

### **3.4.4 Surface area**

#### **3.4.4.1 N<sub>2</sub> adsorption-desorption**

The specific surface area is determined by physical adsorption of the unreactive N<sub>2</sub> gas on solid surface. When the relative pressure is increased, more gas molecules adsorb on the surface and cover the entire surface. The number of gas molecules is recorded from the volume adsorbed and used to determine the area of the accessible surface.

In this work, the electrodes were cut into small pieces and degassed in vacuum at 300 °C for 3 h and N<sub>2</sub> adsorption is measured at 77 K. The specific surface area was calculated by Brunauer-Emmett-Teller (BET) method. The Ni foam surface area was subtracted from total surface area to get the surface area per mass of NiCo<sub>2</sub>S<sub>4</sub> active species.

#### **3.4.5 Electrochemical measurements**

Electrochemical measurements including cyclic voltammetry (CV), Galvanostatic charge-discharge (GCD), and electrochemical impedance spectroscopy (EIS), were carried out at room temperature in three-electrode configuration (Figure 3.1) connected to a working station. The potentiostat is used to control the potential of electrodes or control the current passing through the electrodes. The prepared NiCo<sub>2</sub>S<sub>4</sub> electrodes were used as a working electrode. A Pt plate and Ag/AgCl were used as a counter electrode (CE) and a reference electrode (RE), respectively. 2M KOH solution was used as electrolyte. Capacity is the amount of charge stored measured in mAh. The capacity normalized by mass of active material, called specific capacity (Q), is used to compare the performance between electrodes.

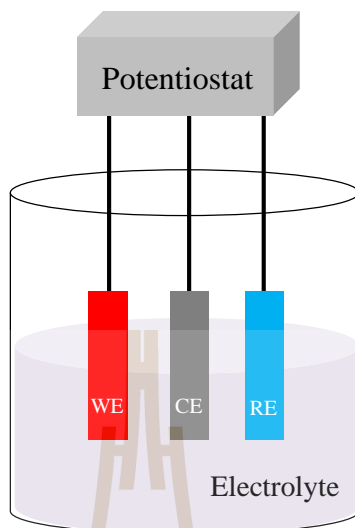


**Figure 3.1** Schematic drawing of three-electrode system with working electrode (WE), counter electrode (CE) and reference electrode (RE)

#### 3.4.5.1 Cyclic voltammetry (CV)

Cyclic voltammetry (CV) is an important electrochemical technique to study the reduction and oxidation processes of active species (Elgrishi *et al.*, 2018). This technique provides both qualitative and quantitative information relating to electrochemical reaction in the active material. In CV measurement, the potential is applied and linearly ramped to working electrode. After reaching the set potential, the potential is ramped in the reverse direction to return to the initial potential. The cycles of triangular ramping in potential should be repeated. The current is measured at the working electrode during the potential scans. Cyclic voltammogram is the plot between current (vertical axis) against the scanned potential (horizontal axis). The specific capacitance can be calculated by using Equation 12 (Chen *et al.*, 2014).

$$C_s = \frac{Q_a + Q_c}{2m\Delta V} \quad (12)$$

where anodic charge ( $Q_a$ ) and cathodic charge ( $Q_c$ ) is obtained from integrated area under the cyclic voltammogram in one cycle of potential scan,  $m$  is mass of active material, and  $\Delta V$  is potential window.

In this work, the cyclic voltammograms were collected in 2 M KOH electrolyte with potential window of 0.5 V using AUTOLAB instrument electrochemical workstation (PGSTAT204) to identify the redox couples of materials. First, the potential scans positively from 0 to +0.5 V versus Ag/AgCl. At potential of 0.5 V, the scan is reversed to initial potential of 0 V. The cyclic voltammogram were carried out at different scan rates including very slow scan rate of 0.5 mV/s to study the capacitance contribution described by Trasatti method (Ardizzone *et al.*, 1990).

#### 3.4.5.2 Galvanostatic charge-discharge (GCD)

In addition to CV, Galvanostatic charge-discharge (GCD) is another reliable technique to determine the capacitance of material. In GCD measurement, the constant current density is applied to the working electrode and the responsive voltage is measured as a function of time. Basically, the working electrode is charged to the set potential and then the discharge process is observed to evaluate the specific capacity following Equation 13 (Ren *et al.*, 2019).

$$Q = \frac{I\Delta t}{m} \quad (13)$$

where  $Q$  is the specific capacity of electrode (mAh/g),  $I$  is the discharge current (mA),  $\Delta t$  is discharge time (h),  $m$  is active mass (g).

In this study, the GCD curves were collected in 2 M KOH electrolyte at current density of 10 A/g with a preset potential of 0.4 V by using AUTOLAB instrument electrochemical workstation (PGSTAT204) to obtain the capacity of all samples and compare their performance. To evaluate the stability of electrodes, the charged-discharged processes were repeated for 1000 cycles at current density of 10 A/g.

#### **3.4.5.3 Electrochemical impedance spectroscopy (EIS)**

It is well-known that the resistance is the ability of a circuit element (resistor, capacitor, inductor etc.) to resist the flow of electrical current following Ohm's law ( $E=IR$ ). In real world, there are more than one circuit element which make more complex behavior. Thus, we use impedance instead of simple resistance. Impedance is like a resistance, but it is not limited by the simplifying properties such as the necessity to follow Ohm's Law at all current and voltage levels. Electrochemical impedance is measured by applying an AC potential with small sinusoidal potential excitation to an electrochemical cell and then measuring the current through that cell. The sinusoidal current response will be phase shift at same frequency. Impedance ( $Z$ ) is composed of a real and an imaginary part. The plot between real part on the X-axis and imaginary part on the Y-axis is called a Nyquist Plot. This plot reveals the information about internal resistance, charge transfer resistance and ion diffusion.

In order to study the electrical conductivity of the prepared electrodes, EIS measurements were performed in 2 M KOH electrolyte in a frequency range from 100 kHz to 0.1 Hz with 10 mV amplitude to obtain a Nyquist Plot.



### 3.4.6 Calculations

#### 3.4.6.1 Computation details

All calculations were carried out using the spin polarized density functional theory (Kohn and Sham, 1965) with periodic boundary conditions as implemented in the Vienna ab-initio simulation package (VASP 5.3) (Kresse and Furthmüller, 1996; Kresse and Furthmüller, 1996; Kresse and Hafner, 1993). The generalized gradient approximation of Perdew-Burke-Ernzerhof functional was used to describe the exchange correlation term (Perdew *et al.*, 1996). We used the Grimme's correction method (DFT-D3) to properly take into account the van der Waals interaction between surface ( $\text{NiCo}_2\text{S}_4$ ) and adsorbates (Grimme, 2006). The nucleus and core electron potentials were treated using the projector augmented wave method (Blöchl, 1994; Kresse and Joubert, 1999) where the valence electrons 3d4s of Fe Co and Ni and 3s3p of S were described by plane-wave basis at 500 eV cutoff. The convergence criteria of the self-consistent field are within  $1.0 \times 10^{-6}$  eV whereas the force convergence of ionic relaxation was set to 0.02 eV/Å.

To study the effect of Fe doping on the electronic structures of  $\text{NiCo}_2\text{S}_4$ , we first optimized the cubic unit cell of  $\text{NiCo}_2\text{S}_4$  using the Monkhorst-Pack (MP) sampling (Monkhorst and Pack, 1976) of  $4 \times 4 \times 4$  k-point mesh in the Brillouin zone. As depicted in Figure 3.2(a), the unit cell contains eight formula units of  $\text{NiCo}_2\text{S}_4$  which corresponds to  $\text{Ni}_8\text{Co}_{16}\text{S}_{32}$ . The calculated lattice parameter of 9.34 Å is consistent with that of the experimental value (9.38 Å) (Bouchard *et al.*, 1965). Then, we replaced one Co or Ni atom with one Fe atom in the unit cell and computed their projected density of states (PDOS) using the tetrahedron smearing method.

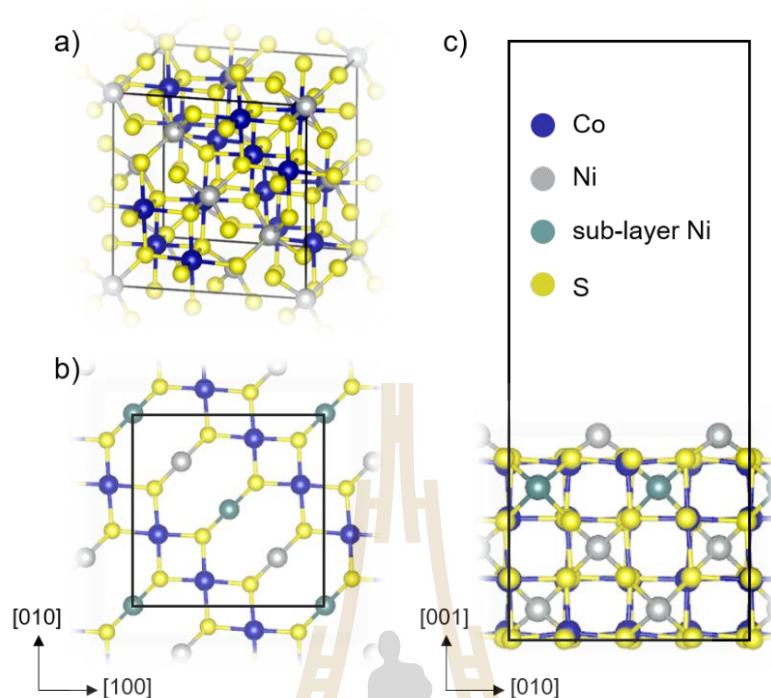


**Figure 3.2** Schematic illustration of a)  $\text{NiCo}_2\text{S}_4$  unit cell, b) top-view, and c) side-view of  $\text{NiCo}_2\text{S}_4$  (100) surface model used in the calculations

To further examine the role of Fe doping on the formation of electrical double layer (EDL) of KOH electrolyte, we used the optimized unit cell to build a slab model of  $\text{NiCo}_2\text{S}_4$  (100) surface with eight-atomic layers as shown in Figure 3.2(b) and (c). The bottom four layers were kept frozen to mimic a bulk-like structure while the others were relaxed. A  $15 \text{ \AA}$  vacuum gap was added in the c direction to avoid the interaction between periodic images. We replaced one Fe atom at the Ni site or Co site to obtain the Fe-doped surfaces. Six  $\text{K}^+$  ions and  $\text{OH}^-$  ions were added to the surface to form the EDL on the surface. Their internal coordinates were relaxed using  $4 \times 4 \times 1$  k-point sampling of MP scheme where the interactions,  $E_{\text{ad}}$ , were calculated according to the given equation

$$E_{\text{ad}} = E_{\text{EDL}} - (6E_{\text{KOH}} + E_{\text{slab}})$$

where  $E_{\text{EDL}}$  is the total energy of the system when six KOH are adsorbed on the slab,  $E_{\text{KOH}}$  and  $E_{\text{slab}}$  are the total energy of free adsorbate and the clean or doped (100) surface before adsorption, respectively.

### 3.5 References

- Ardizzone, S., Fregonara, G., and Trasatti, S. (1990) "Inner" and "outer" active surface of RuO<sub>2</sub> electrodes. **Electrochimica Acta**. 35: 263-267.
- Blöchl, P. E. (1994) Projector augmented-wave method. **Physical Review B**. 50: 17953-17979.
- Bouchard, R. J., Russo, P. A., and Wold, A. (1965) Preparation and Electrical Properties of Some Thiospinels. **Inorganic Chemistry**. 4: 685-688.
- Chen, S. M., Ramachandran, R., Mani, V., and Saraswathi, R. (2014). Recent Advancements in Electrode Materials for the High-performance Electrochemical Supercapacitors: A review. **International Journal of Electrochemical Science**. 9: 4072-4085.
- Elgrishi, N., Rountree, K. J., McCarthy, B. D., Rountree, E. S., Eisenhart, T. T., and Dempsey, J. L. (2018). A Practical Beginner's Guide to Cyclic Voltammetry. **Journal of Chemical Education**. 95: 197-206.
- Grimme, S. (2006). Semiempirical GGA-type density functional constructed with a long-range dispersion correction. **Journal of Computational Chemistry**. 27: 1787-1799.

- Kim, B. K., Sy, S., Yu, A., and Zhang, J. (2015). **Handbook of Clean Energy and Energy systems**. John Wiley & Son, Ltd.
- Kohn, W. and Sham, L. J. (1965). Self-Consistent Equations Including Exchange and Correlation Effects. **Physical Review**. 140: A1133-A1138.
- Kresse, G. and Furthmüller, J. (1996). Efficient iterative schemes for ab initio total-energy calculations using a plane-wave basis set. **Physical Review B**. 54: 11169-11186.
- Kresse, G. and Furthmüller, J. (1996). Efficiency of ab-initio total energy calculations for metals and semiconductors using a plane-wave basis set. **Computational Materials Science**. 6: 15-50.
- Kresse, G. and Hafner, J. (1993). Ab initio molecular dynamics for liquid metals. **Physical Review B**. 47: 558-561.
- Kresse, G. and Joubert, D. (1999). From ultrasoft pseudopotentials to the projector augmented-wave method. **Physical Review B**. 59: 1758-1775.
- Monkhorst, H. J. and Pack, J. D. (1976). Special points for Brillouin-zone integrations. **Physical Review B**. 13: 5188-5192.
- Perdew, J. P., Burke, K., and Ernzerhof, M. (1996). Generalized Gradient Approximation Made Simple. **Physical Review Letters**. 77: 3865-3868.
- Ren, X., Du, Y., Song, M., Chen, Y., Zhou, Y., Ma, F., and Wan, J. (2019). Facile preparation of mesoporous NiCo<sub>2</sub>S<sub>4</sub> microaggregates constructed by nanoparticles via puffing NiCo<sub>2</sub>O<sub>4</sub> cubes for high performance asymmetric supercapacitors. **Journal of Alloys and Compounds**. 806: 1481-1490.
- West, A. R. (2014). **Solid state chemistry and its applications** (2nd ed.). John Wiley & Sons, Ltd.

# CHAPTER IV

## RESULTS AND DISCUSSION

### 4.1 Sample preparation

In this work, all samples of  $\text{NiCo}_2\text{S}_4$  with  $\text{FeCl}_3$  additives including 0Fe-NCS, 0.25Fe-NCS, 0.5Fe-NCS, 1Fe-NCS, 1.5Fe-NCS and 2Fe-NCS (0, 0.12, 0.25, 0.5, 0.75, and 1 mmol of  $\text{FeCl}_3$ ), were synthesized by a simple one-step hydrothermal method. The hydrothermal technique for this synthesis involves three main mechanisms: hydrolysis, coprecipitation, and ion-exchange. The hydrolyzation of thiourea generates sulfur ( $\text{S}^{2-}$ ) and ammonia. Subsequently,  $\text{Ni}^{2+}$  and  $\text{Co}^{2+}$  from metal nitrates are coprecipitated to form Ni-Co hydroxides on Ni foam. The Ni-Co hydroxides are further converted to  $\text{NiCo}_2\text{S}_4$  product by reacting with  $\text{S}^{2-}$  (Wang *et al.*, 2016).

### 4.2 Sample characterizations

#### 4.2.1 X-ray diffraction (XRD)

Figure 4.1(a) shows X-ray diffraction (XRD) patterns of the samples 0Fe-NCS, 0.25Fe-NCS, 0.5Fe-NCS, 1Fe-NCS, 1.5Fe-NCS and 2Fe-NCS on Ni foam. Note that the electrodes (not the powder) were directly used in XRD measurement which may cause some peak shifts. The two strong diffractions at  $45^\circ$  and  $52^\circ$  belong to Ni foam. The five diffraction peaks at  $27^\circ$ ,  $31^\circ$ ,  $38^\circ$ ,  $50^\circ$  and  $55^\circ$  correspond to (220), (311), (400), (511) and (440) diffraction planes of the cubic  $\text{NiCo}_2\text{S}_4$  phase (PDF 43-1477), respectively (Pu *et al.*, 2014; Wang *et al.*, 2016). To better detect the reflections from

intended  $\text{NiCo}_2\text{S}_4$  phase, additional XRD scans with finer step and longer collection time were collected as shown in Figure 4.1(b).

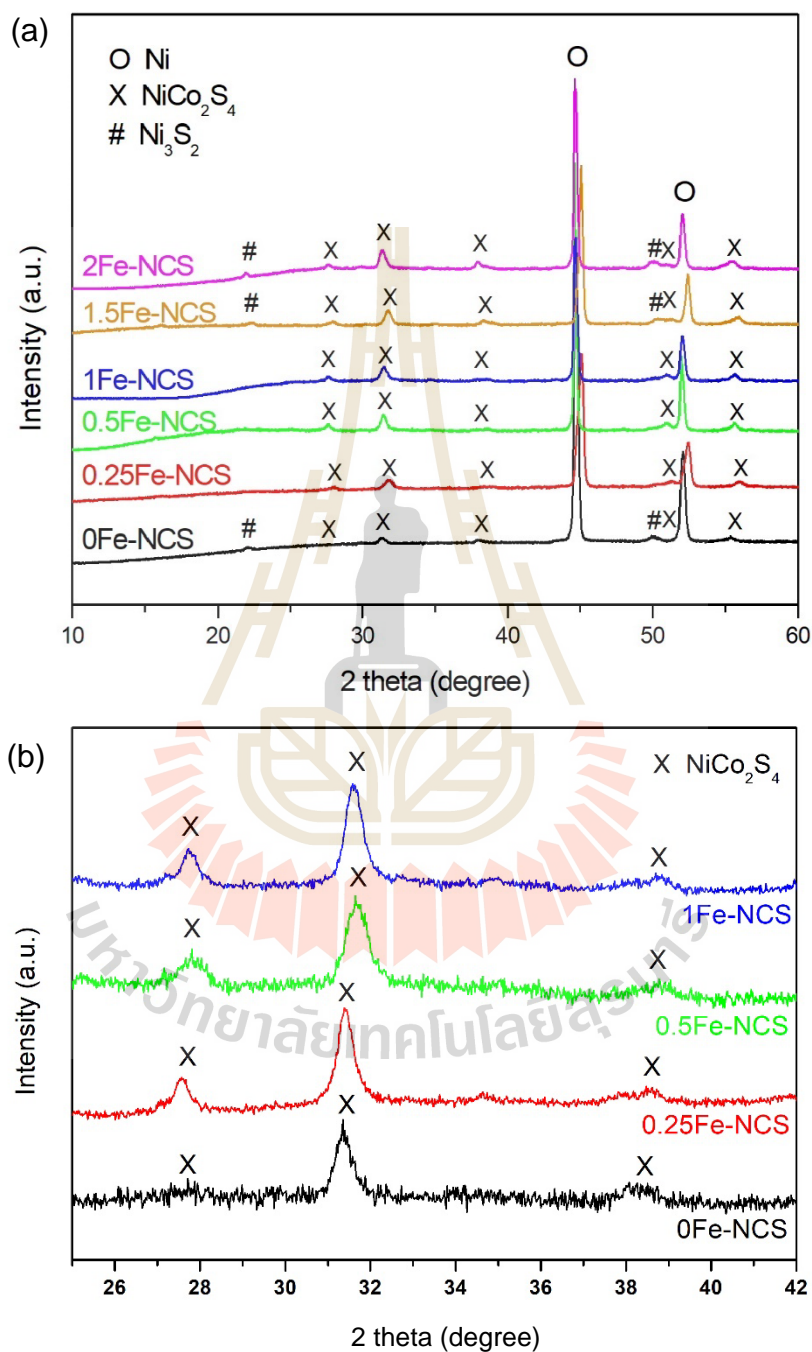
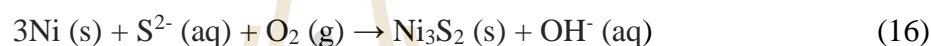


**Figure 4.1** XRD patterns of samples on Ni foam. (a) normal scan (b) finer scan in 2 theta range 25 to 42°

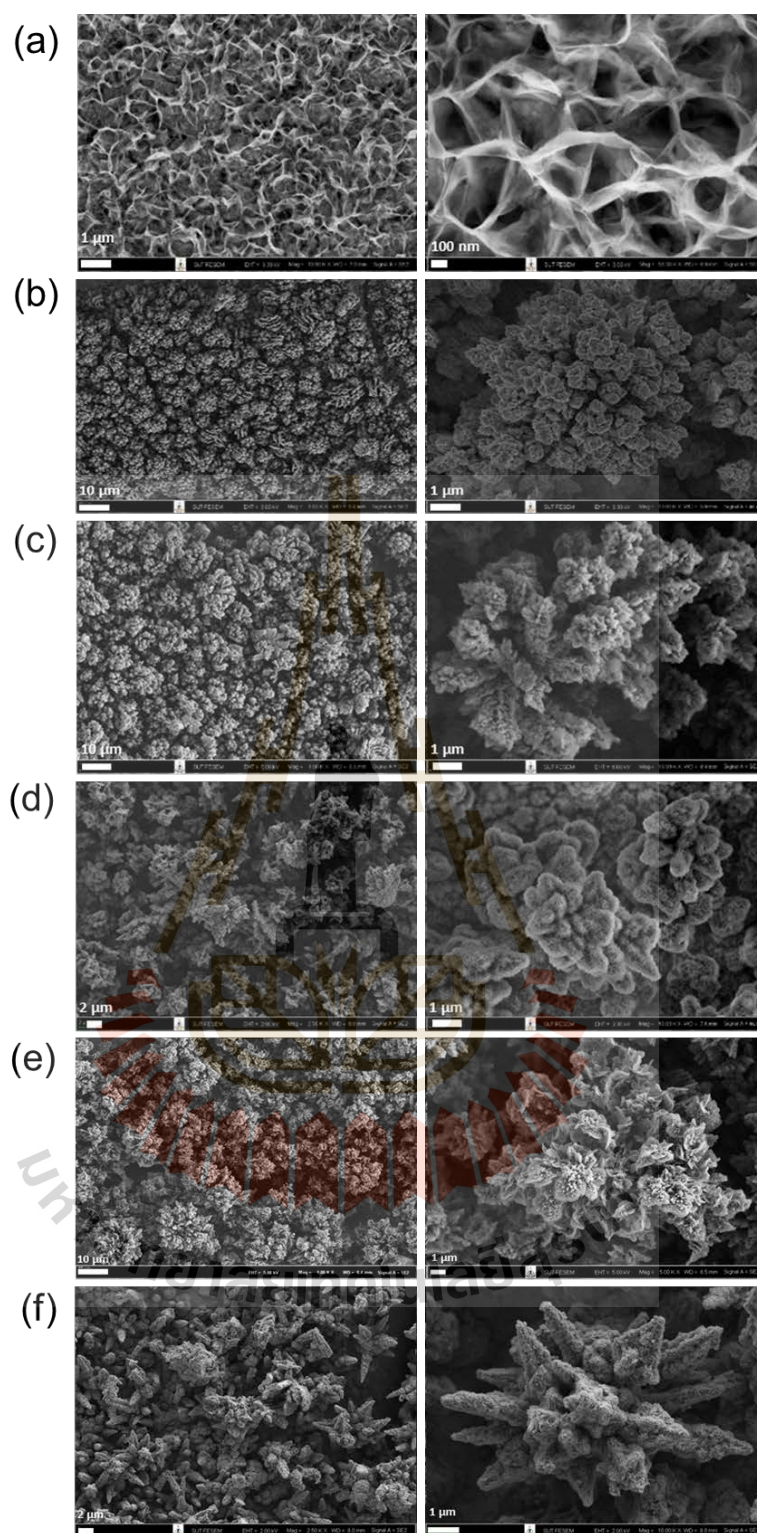
It is noted that some additional peaks at 21.7° and 50.0° found in 0Fe-NCS, 1.5Fe-NCS and 2Fe-NCS samples can be indexed to Ni<sub>3</sub>S<sub>2</sub> impurity. The formation of Ni<sub>3</sub>S<sub>2</sub> may come from the interfacial reaction between the outer surface of Ni foam and sulfur ion from thiourea during the hydrothermal reaction (Krishnamoorthy *et al.*, 2014; Jinlong *et al.*, 2017). The possible chemical reactions are shown by the equation 14, 15 and 16:



The XRD patterns demonstrate that NiCo<sub>2</sub>S<sub>4</sub> were successfully synthesized in 0.25Fe-NCS, 0.5Fe-NCS and 1Fe-NCS samples. No impurities containing Fe are observed.

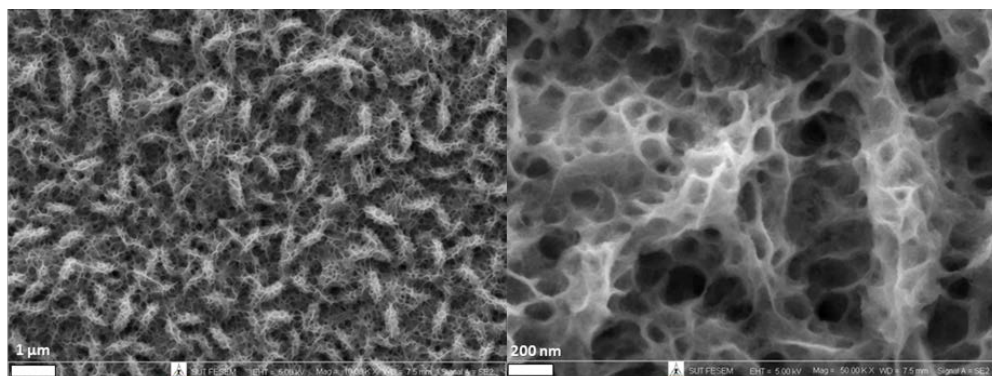
#### 4.2.2 Field emission scanning electron microscopy (FESEM)

Morphology of the obtained samples was investigated by FESEM technique. The effects of Fe addition on morphologies of the samples are clearly seen in Figure 4.2. The 0Fe-NCS sample shows nanosheet feature which is similar to the previous report (Wang *et al.*, 2016). However, these features are destroyed when FeCl<sub>3</sub> is added. Then, we prepared the sample with NaCl addition to check whether Cl<sup>-</sup> from FeCl<sub>3</sub> affected the shape or not. Interestingly, the obtained sample possess a similar 2D network feature (Figure 4.3).



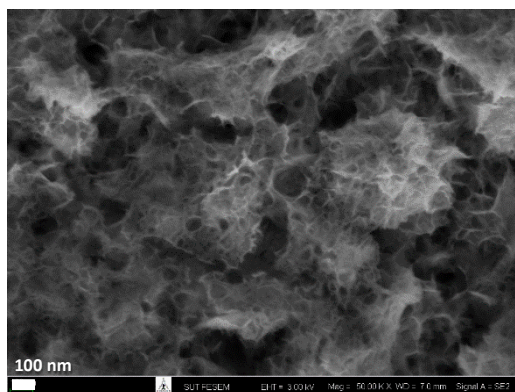
**Figure 4.2** FESEM image at low magnification (left) and high magnification (right) of (a) 0Fe-NCS (b) 0.25Fe-NCS (c) 0.5Fe-NCS (d) 1Fe-NCS (e) 1.5Fe-NCS and (f) 2Fe-NCS.





**Figure 4.3** FESEM image of NaCl-added NiCo<sub>2</sub>S<sub>4</sub>.

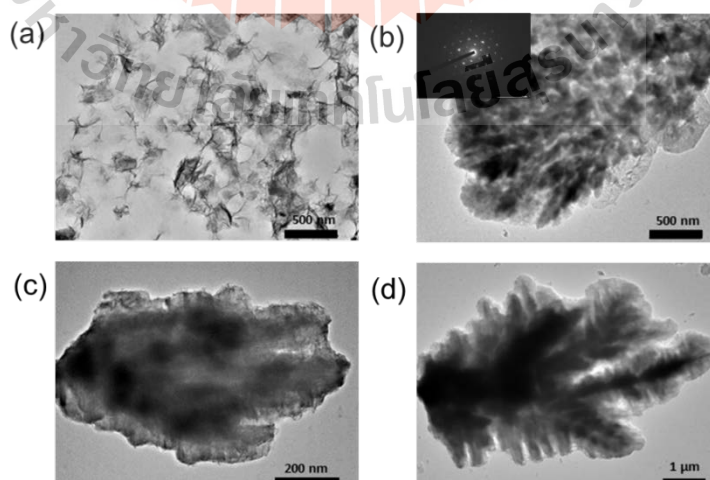
In hydrothermal synthesis of NiCo<sub>2</sub>S<sub>4</sub>, the only ionic compound used as an additive in many publications is NH<sub>4</sub>F (Chen *et al.*, 2017; Lin *et al.*, 2015; Lu *et al.*, 2016). It was concluded that NH<sub>4</sub>F increases the acidity of the system and activates surface of the samples which benefit the growth of particles with high dimensions (2D-3D). Similarly, Fe<sup>3+</sup> is well known to form an aqua acid, [Fe(H<sub>2</sub>O)<sub>6</sub>]<sup>3+</sup>, making the system more acidic. In fact, pH of the solution before hydrothermal synthesis with FeCl<sub>3</sub> addition was equal to three. Overall, the presence of [Fe(H<sub>2</sub>O)<sub>6</sub>]<sup>3+</sup> destroys 2D nanosheets and give rise to agglomeration of coral-like particles. To compare, we prepared the sample by adjusting the pH with HCl solution to pH 3. The result as shown in Figure 4.4 is different from the morphology of 1Fe-NCS sample. Therefore, Fe<sup>3+</sup> plays an important role on the samples' morphology.



**Figure 4.4** FESEM image of  $\text{NiCo}_2\text{S}_4$  adjusted to pH 3 by HCl.

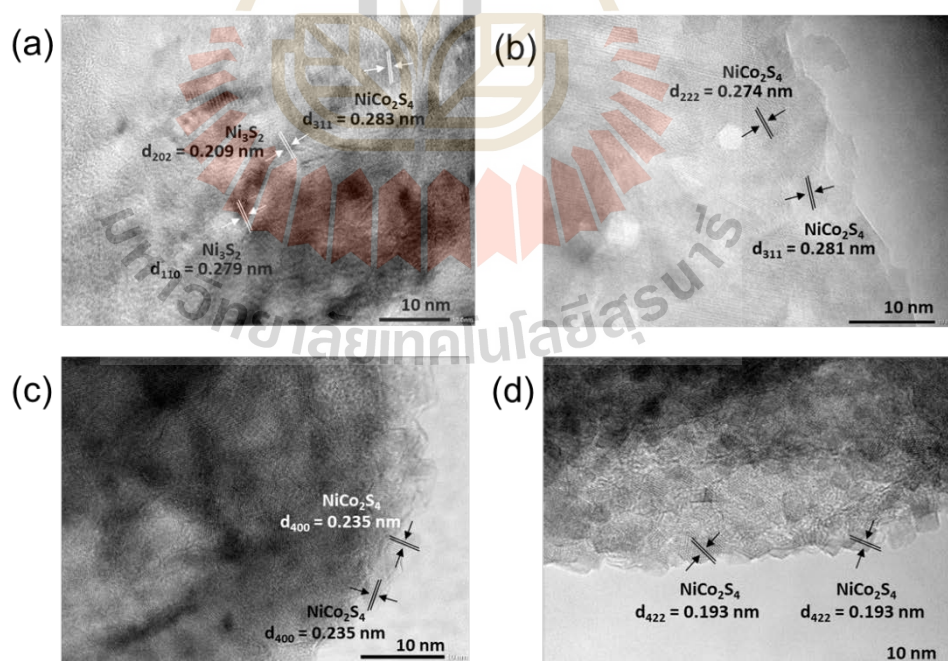
#### 4.2.3 Transmission electron microscopy (TEM)/Energy dispersive X-ray spectroscopy (EDS)

We performed TEM imaging of samples peeled from Ni foam using ultrasonication in ethanol. TEM image of 0Fe-NCS (Figure 4.5(a)) reveals the thin nanosheets which is consistent with the SEM image while the core-shell like features are obtained in samples containing Fe as shown in Figure 4.5(b)-(d). The TEM images suggest that the particles become denser with increasing Fe-content.



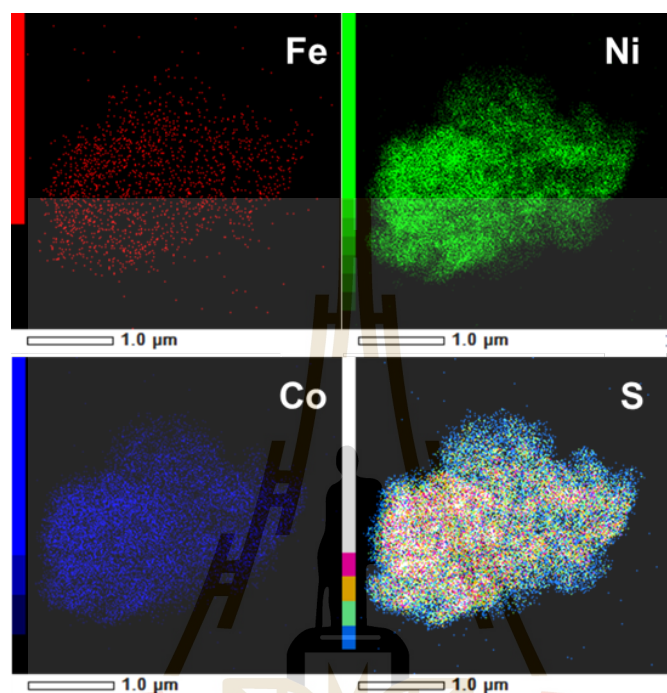
**Figure 4.5** TEM image of (a) 0Fe-NCS (b) 0.25Fe-NCS (c) 0.5Fe-NCS and (d) 1Fe-NCS

Figure 4.6 shows close-up TEM images of 0Fe-NCS and the shell region of 0.25Fe-NCS, 0.5Fe-NCS and 1Fe-NCS samples. The crystalline nature of samples is confirmed by the interlaced crystalline directions. We use ImageJ program to determine the d-spacing of each lattice fringe. The obtained d-spacing in all samples match well with the interplanar spacing of  $\text{NiCo}_2\text{S}_4$ . For 0Fe-NCS, lattice fringes belonging to  $\text{Ni}_3\text{S}_2$  are also observed which confirms the results from XRD patterns. Additionally, the well-defined lattice fringe observed in Fe-added samples indicates that the crystallinity gradually increases with Fe content, although the polycrystalline nature does not change. The selected area electron diffraction (SAED) pattern with some clear spots of 0.25Fe-NCS sample as shown in Figure 4.5b (inset), confirmed the crystallinity nature of materials.



**Figure 4.6** Close-up TEM image of (a) 0Fe-NCS (b) 0.25Fe-NCS (c) 0.5Fe-NCS and (d) 1Fe-NCS

The compositions of all elements including Ni, Co, S, and Fe in Fe-added samples were confirmed by EDS technique as shown in Figure 4.7-4.9. They are uniformly distributed in the samples.



**Figure 4.7** EDS elemental mapping of 0.25Fe-NCS sample

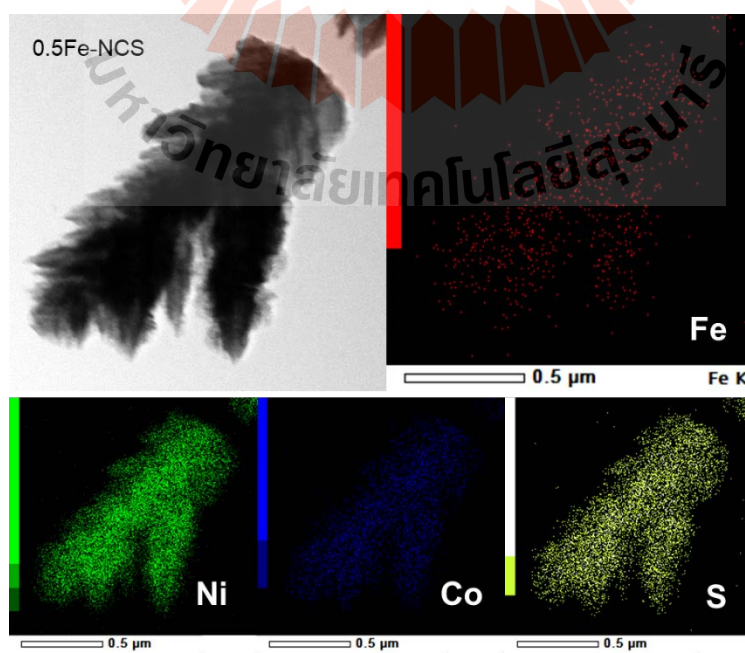


**Figure 4.8** EDS elemental mapping of 0.5Fe-NCS sample.

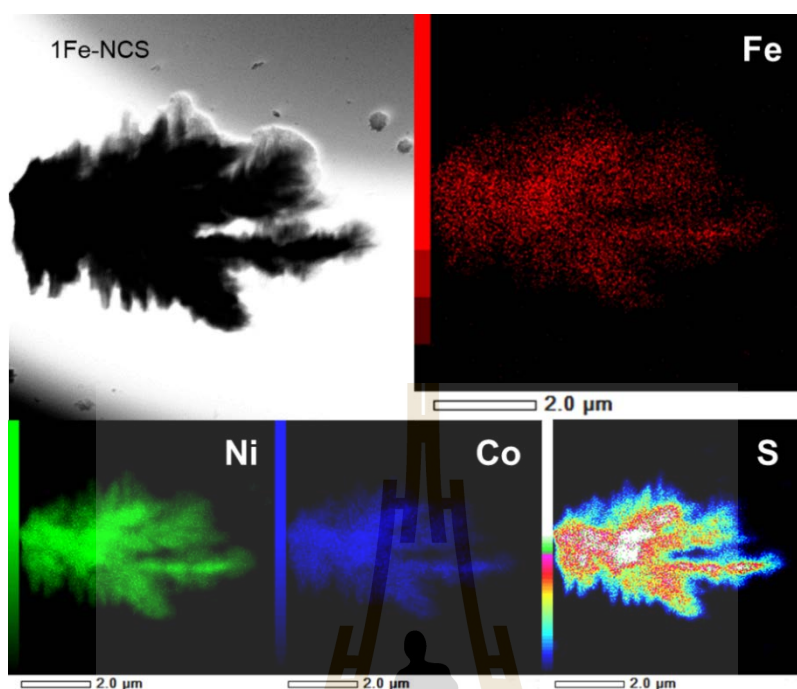


**Figure 4.9** EDS elemental mapping of 1Fe-NCS sample

#### 4.2.4 Inductively coupled plasma-optical emission spectrometry (ICP-OES)

The Fe contents in 0.25Fe-NCS, 0.5Fe-NCS and 1Fe-NCS sample are estimated to be 0.89%, 1.16% and 1.61% by mole relative to Ni content, which are much lower than the initial ratio. Fe in the sample can exist in two possible form. First is the formation of  $\text{FeCo}_2\text{S}_4$  which is mixed with  $\text{NiCo}_2\text{S}_4$ . However, there are no peaks of  $\text{FeCo}_2\text{S}_4$  phase presenting in XRD pattern (Figure 4.1), thus, the more probable scenario is with Fe being doped into the  $\text{NiCo}_2\text{S}_4$  lattice.

### 4.2.5 X-ray photoelectron spectroscopy (XPS)

X-ray photoelectron spectroscopy is employed to confirm the oxidation state of elements. The XPS spectra of Ni and Co are fitted by the Gaussian method. The Ni 2p spectrum (Figure 4.10) is deconvoluted into four peaks with two spin-orbit doublets and two shakeup satellites (marked as “sat.”). The binding energy at around 856 eV in Ni 2p<sub>3/2</sub> and 873 eV in Ni 2p<sub>1/2</sub> are assigned to Ni<sup>2+</sup>. While the binding energy at around 857 eV in Ni 2p<sub>3/2</sub> and 876 eV in Ni 2p<sub>1/2</sub> correspond to Ni<sup>3+</sup>. The binding energies of samples are shown in Table 4.1. These results are in good agreement with previous report of NiCo<sub>2</sub>S<sub>4</sub> (Wang *et al.*, 2016).

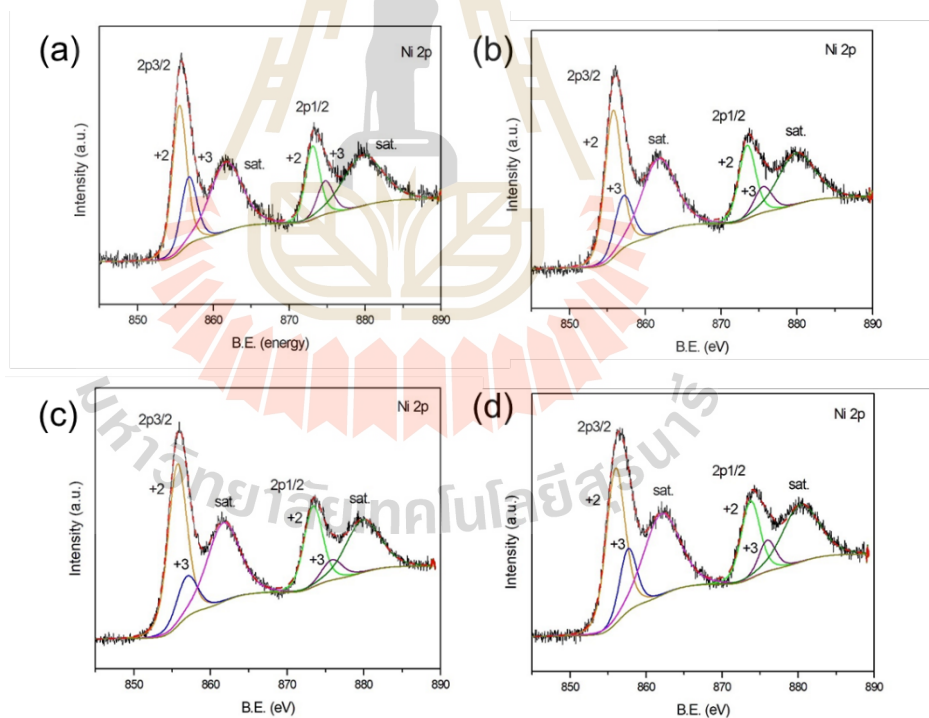


**Figure 4.10** Ni 2p spectrum of (a) 0Fe-NCS (b) 0.25Fe-NCS (c) 0.5Fe-NCS and (d) 1Fe-NCS.

**Table 4.1** Binding energies and Ni<sup>2+</sup> to Ni<sup>3+</sup> ratio of NiCo<sub>2</sub>S<sub>4</sub> samples.

Sample	Binding energy (eV)				Ni <sup>2+</sup> to Ni <sup>3+</sup> ratio
	Ni <sup>2+</sup>		Ni <sup>3+</sup>		
	2p <sub>3/2</sub>	2p <sub>1/2</sub>	2p <sub>3/2</sub>	2p <sub>1/2</sub>	
0Fe-NCS	855.5	873.1	856.7	874.7	1 : 0.51
0.25Fe-NCS	855.7	873.4	857.1	875.6	1 : 0.38
0.5Fe-NCS	855.7	873.4	856.9	875.9	1 : 0.28
1Fe-NCS	855.9	873.7	857.6	875.9	1 : 0.36

Moreover, we found that Ni<sup>3+</sup> content slightly decreases in samples containing Fe as seen in Table 4.1. It is believed that Ni<sup>3+</sup> are converted to Ni<sup>2+</sup> which is similar to previous study in Fe-substituted NiCo<sub>2</sub>O<sub>4</sub> (Yuan *et al.*, 2019), though the change we observed is less significant.

The Co 2p spectrum (Figure 4.11) of 0Fe-NCS sample can be well-fitted with two spin-orbit doublets and two shakeup satellites, the fitting peak of 799.9 eV and 796.2 eV are attributed to Co<sup>3+</sup>. The binding energy at 781.4 eV and 797.0 eV are associated with Co<sup>2+</sup>. Moreover, the spin-orbit splitting value of Co 2p<sub>1/2</sub> and Co 2p<sub>3/2</sub> in 0Fe-NCS sample is 15.6 eV. The spin-orbit splitting value is over 15 eV, suggesting the coexistence of Co<sup>2+</sup> and Co<sup>3+</sup> (Yang *et al.*, 2015). The coexistence of Co<sup>2+</sup> and Co<sup>3+</sup> has been reported in many works (Chen *et al.*, 2017; Pu *et al.*, 2014; Yang *et al.*, 2015). Unfortunately, the Co 2p spectra of other samples with FeCl<sub>3</sub> addition cannot be fit due to the overlapping between photoemission of Co and auger of Fe. Nevertheless, the positions and shapes of spectra are roughly the same.

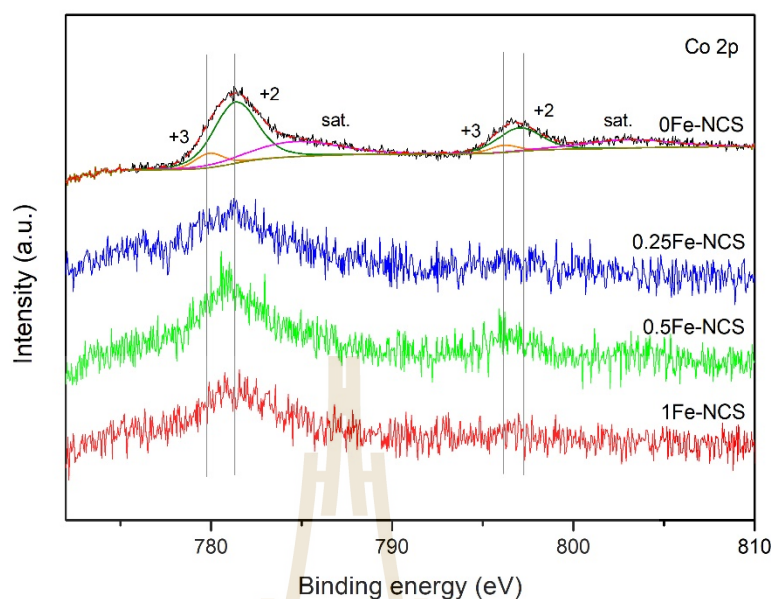


**Figure 4.11** Co 2p spectrum of all samples.

In the S 2p spectrum of 0.25Fe-NCS sample (Figure 4.12(b)), it can be fitted into two main peaks at 162.1 eV and 163.2 eV and one shakeup satellite. The component at 163.2 eV (S 2p<sub>3/2</sub>) is the binding energy of metal-sulfur bond, Ni-S and Co-S. While the peak located at 162.1 (S 2p<sub>1/2</sub>) is attributed to sulfur ion in low coordination at surface (Wang *et al.*, 2016; Chen *et al.*, 2017; Pu *et al.*, 2014). The S 2p spectra of other samples with FeCl<sub>3</sub> addition (Figure 4.12) are similar to 0.25Fe-NCS spectrum. In case of 0Fe-NCS sample as shown in Figure 4.12(a), the binding energy at around 169 eV corresponds to sulfate compound (Moulder *et al.*, 1992). This may attribute to surface oxidation.



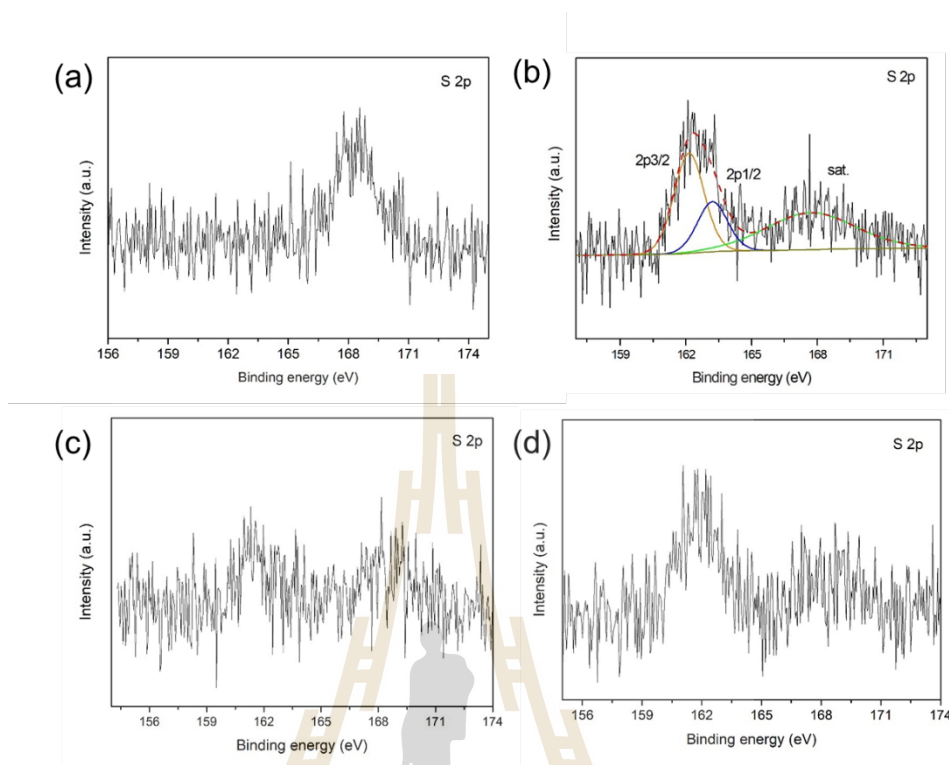


**Figure 4.12** S 2p spectrum of (a) 0Fe-NCS (b) 0.25Fe-NCS (c) 0.5Fe-NCS and (d) 1Fe-NCS.

To deal with the overlapping with Auger of other atom and surface oxidation in XPS technique, we additionally employed XAS technique to determine the valence states of Fe and S.

#### 4.2.6 X-ray absorption near edge spectroscopy (XANES)

X-ray absorption near edge spectroscopy is performed to determine the chemical states of the elements. The oxidation state of Fe in the samples can be interpreted by edge position in Fe K-edge XANES spectra. Figure 4.13 displays the spectra of Fe-doped samples and standards FeO ( $\text{Fe}^{2+}$ ) and  $\text{Fe}_2\text{O}_3$  ( $\text{Fe}^{3+}$ ) for comparison. The edge energies of FeO and  $\text{Fe}_2\text{O}_3$  standards are  $\sim 7120$  eV and  $\sim 7125$  eV, respectively (Latif *et al.*, 2018; Phokha *et al.*, 2016). In case of Fe-added samples, the edge energies of 0.25Fe-NCS, 0.5Fe-NCS, and 1Fe-NCS are 7126.4, 7126.4, and 7127.4 eV, respectively. It can be seen that all samples have edge energies closed to  $\text{Fe}^{3+}$  standard, indicating that the oxidation state of Fe in the Fe-added samples are 3+.

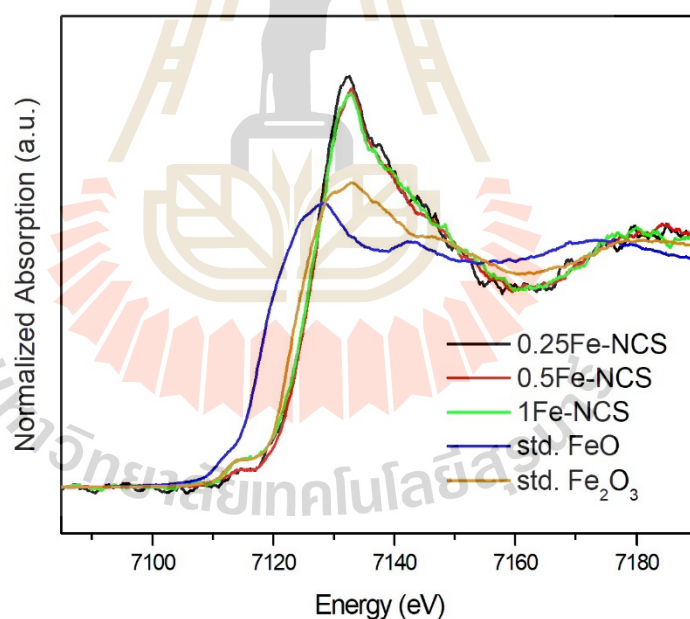


**Figure 4.13** Fe K-edge XANES spectra of 0.25Fe-NCS, 0.5Fe-NCS, and 1Fe-NCS

The sulfur component in  $\text{NiCo}_2\text{S}_4$  samples is investigated by S K-edge XANES as shown in Figure 4.14. The edge energy is proportional to oxidation state of sulfur, ranging from 2469 eV for  $\text{S}^{2-}$  to 2483 eV for  $\text{S}^{6+}$  (Kornienko *et al.*, 2015; Bonnin-

Mosbah *et al.*, 2002) For sample without FeCl<sub>3</sub> addition (0Fe-NCS), the edge position is 2470.2 eV. In case of Fe-added samples, the edge energies of 0.25Fe-NCS, 0.5Fe-NCS, and 1Fe-NCS are 2469.9, 2470.0, and 2470.0 eV, respectively. It can be seen that all samples have edge energies closed to S<sup>2-</sup> standard, indicating the oxidation state of sulfur in the samples are 2- as expected.

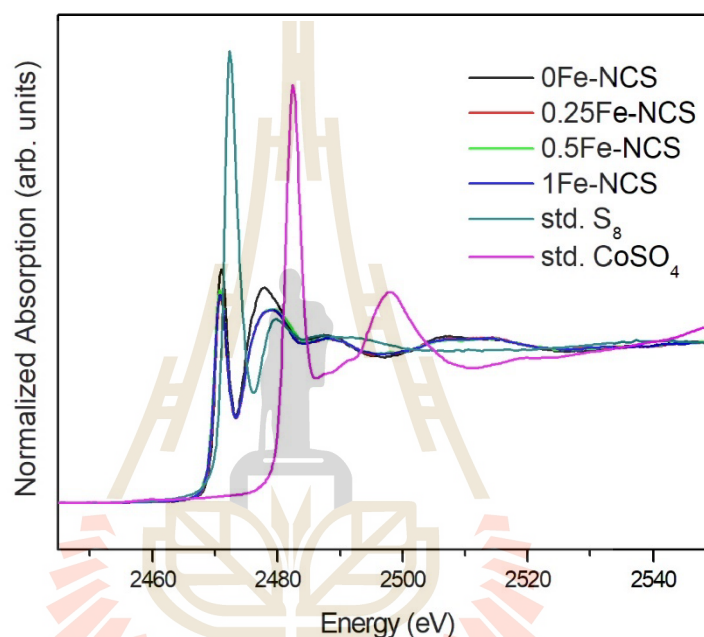


**Figure 4.14** S K-edge XANES spectra of 0Fe-NCS, 0.25Fe-NCS, 0.5Fe-NCS, and 1Fe-NCS.

#### 4.2.7 N<sub>2</sub> adsorption-desorption

Surface area is one of the factors that affect the electrochemical performance of materials. To study the surface properties, adsorption-desorption isotherms of N<sub>2</sub> were carried out at 77 K as shown in Figure 4.15. All curves belong to type III isotherm with H2 hysteresis loop, indicating the mesoporous structure of samples.

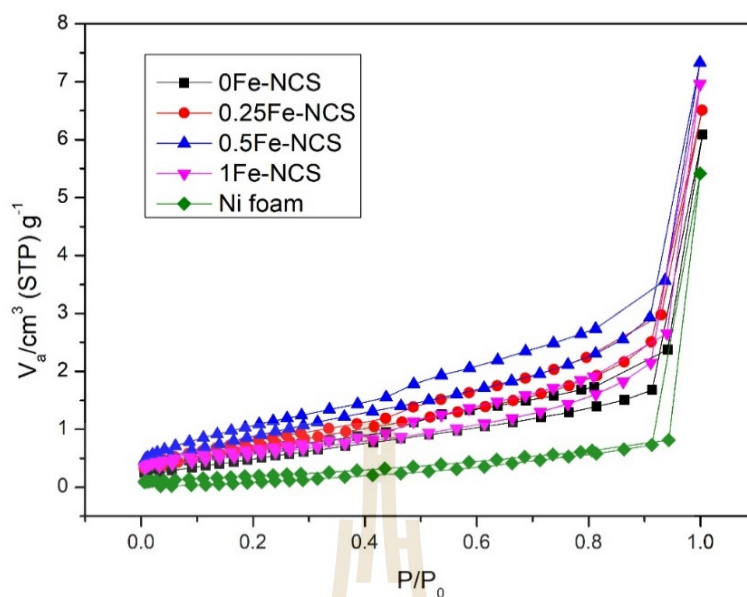


**Figure 4.15** N<sub>2</sub> adsorption/desorption isotherm of NiCo<sub>2</sub>S<sub>4</sub> samples and Ni foam.

**Table 4.2** Surface properties of NiCo<sub>2</sub>S<sub>4</sub> samples and Ni foam.

Sample	Surface area (m <sup>2</sup> /g)	Calculated surface area per mass of NiCo <sub>2</sub> S <sub>4</sub> (m <sup>2</sup> /g)	Pore volume (cm <sup>3</sup> /g)	Pore diameter (nm)
0Fe-NCS	2.13	82.70	0.00838	15.771
0.25Fe-NCS	2.86	77.84	0.00918	12.835
0.5Fe-NCS	3.61	108.68	0.01064	11.784
1Fe-NCS	2.17	99.11	0.00998	18.430
Ni foam	0.86	0.86	0.00758	35.257

From Table 4.2, the BET surface areas of all electrodes (including NiCo<sub>2</sub>S<sub>4</sub> on Ni foam substrate) are similar. The surface area per mass of NiCo<sub>2</sub>S<sub>4</sub> is calculated by subtracting the Ni foam surface area and dividing with actual mass of material. The

surface areas of  $\text{NiCo}_2\text{S}_4$  are in the range of 80-110  $\text{m}^2/\text{g}$ , which are similar to other hydrothermally prepared  $\text{NiCo}_2\text{S}_4$  electrodes (Wei *et al.*, 2017; Peng *et al.*, 2013; Liu *et al.*, 2017).

### 4.3 Electrochemical measurements

The electrochemical performance of  $\text{NiCo}_2\text{S}_4$  electrodes has been evaluated by cyclic voltammetry (CV) and galvanostatic charge-discharge (GCD) in 2 M KOH solution using three electrode system. The  $\text{NiCo}_2\text{S}_4$  samples on Ni foam (0Fe-NCS, 0.25Fe-NCS, 0.5Fe-NCS and 1Fe-NCS) were directly employed as binder-free working electrode. Mass loading on 1.5Fe-NCS and 2Fe-NCS samples is very low compared with other electrodes due to the corrosion of electrodes and the presence of impurity with high amount of  $\text{FeCl}_3$  acid. Thus, they are not further characterized.

#### 4.3.1 Cyclic voltammetry (CV)

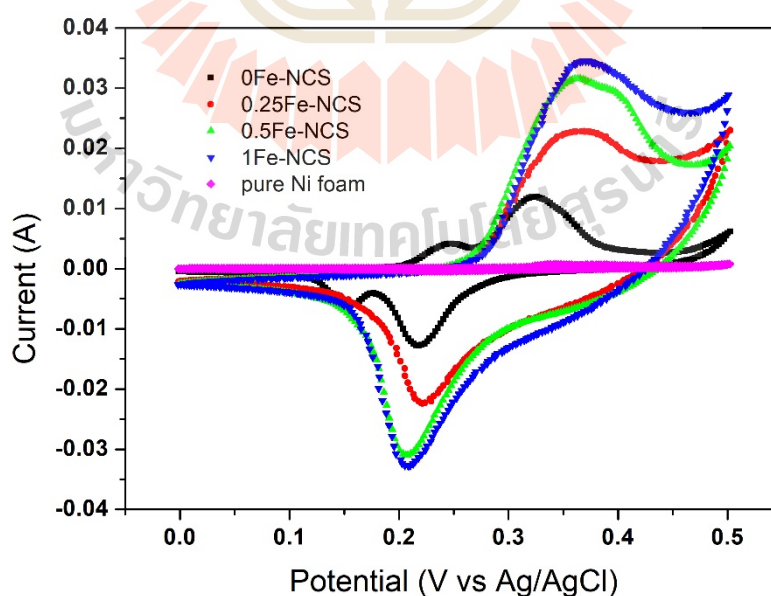
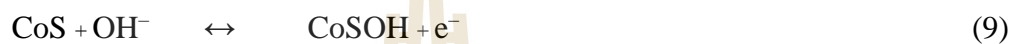


**Figure 4.16** CV curves of all samples at scan rate of 5 mV/s.

The CV curves of samples with the potential window ranging from 0 to 0.5 V at scan rate of 5 mV/s are shown in Figure 4.16, the anodic peak for oxidation process appears at 0.35 V and the cathodic peak for reaction process presents at around 0.20 V which are similar to previous works (Huang *et al.*, 2016; Shen *et al.*, 2015; Chen *et al.*, 2018). A pair of redox reaction peaks indicates that capacitance contribution is mainly from Faradaic reaction of  $\text{Co}^{2+}/\text{Co}^{3+}/\text{Co}^{4+}$  and  $\text{Ni}^{2+}/\text{Ni}^{3+}$  redox couples in KOH solution as shown in equation 9, 10 and 11 (Yang *et al.*, 2015; Gao and Huang, 2017):



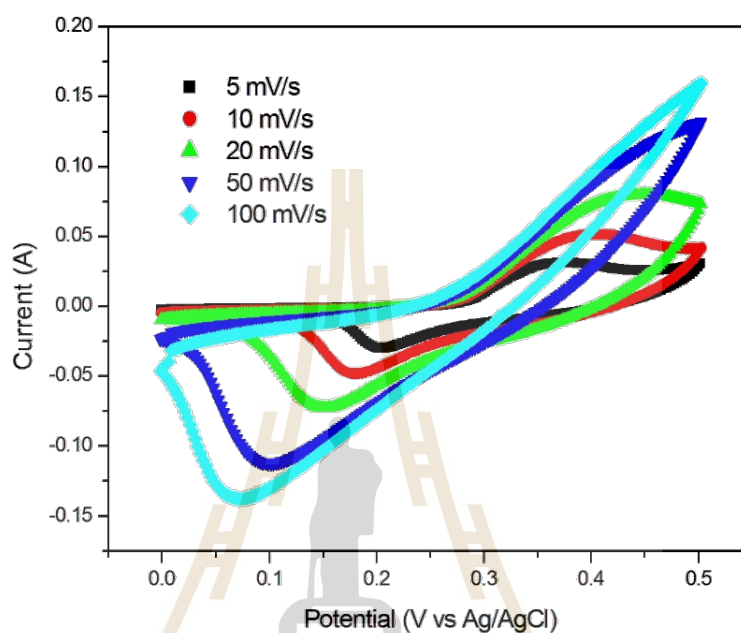
There are some extra peaks in CV curve of 0Fe-NCS corresponding to the redox reaction of  $\text{Ni}_3\text{S}_2$  in KOH solution by equation 17 (Krishnamoorthy *et al.*, 2014; Jinlong *et al.*, 2017).



The 1Fe-NCS electrode shows the most remarkable peaks and larger area within the curves when compare the CV curves under the same scan rate, indicating the highest capacitance. While CV curve of a pure Ni foam used as current collector is almost a straight line, indicating that the capacitance contribution from Ni foam is negligible. The capacitance values reflect their energy storage performance. This can be further confirmed by GCD measurements.

Figure 4.17 shows the CV curves of prepared 1Fe-NCS electrode at different scan rates of 5, 10, 20, 50 and 100 mV/s. The shift for oxidation peak toward higher

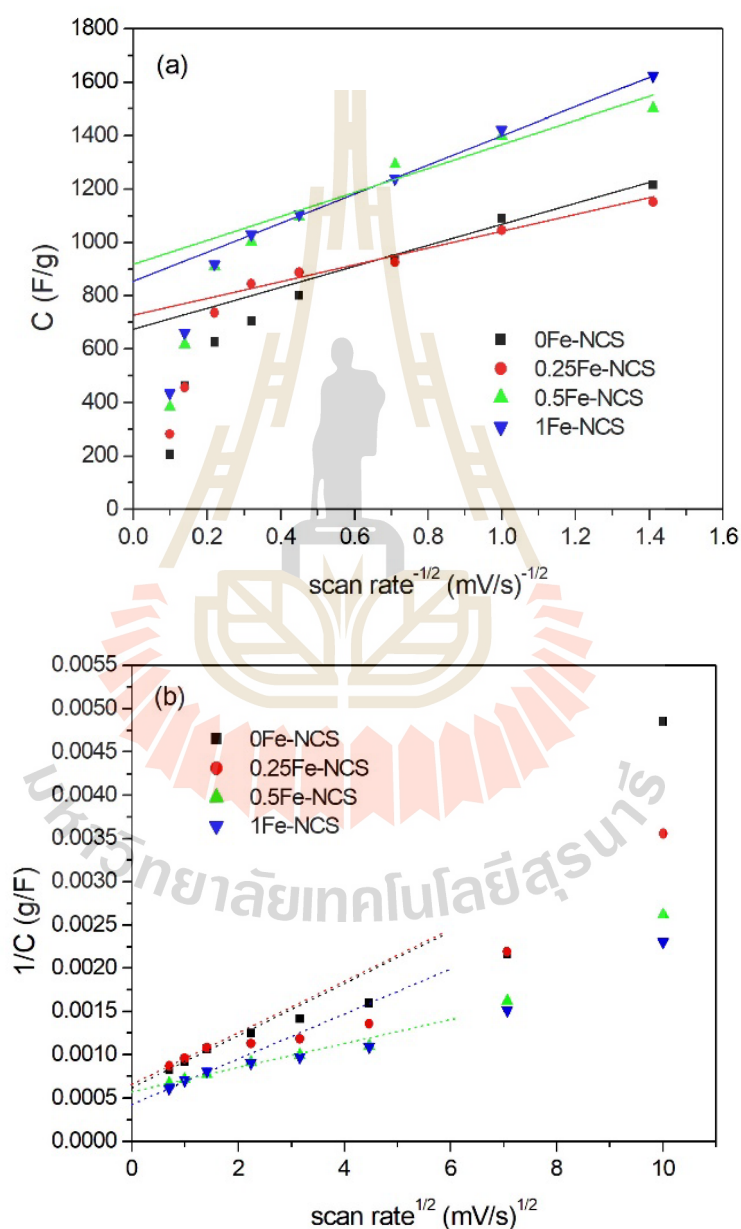
potential appears with increase of scan rate. Meanwhile, the shift for reduction peak toward lower potential also occurs due to the fast redox processes at the electrode-electrolyte interface (Chen *et al.*, 2017).



**Figure 4.17** CV curves of 1Fe-NCS electrode at various scan rates.

It is interesting to know how Fe affects the capacitive behavior. The contribution from surface capacitance ( $C_{\text{sur}}$ ) and diffusion-controlled capacitance ( $C_{\text{diff}}$ ) can be separated by Trasatti method (Ardizzone *et al.*, 1990; Duay *et al.*, 2013; Shao *et al.*, 2015). To do this, CV measurements were performed with a series of scan rate from 0.5 to 100 mV/s. Two plots as shown in Figure 4.18 were used to extrapolate the capacitance at scan rate of zero and infinity. Here, the semi-infinite linear diffusion is assumed, so we expect a linear relationship between capacitance and the inverse square root of scan rate. Similarly, the inverse capacitance decreases linearly with square root of scan rate. However, the plots deviate from linearity at high scan rates because of the ohmic resistance and irreversible redox processes (Zhou *et al.*, 2017). With sufficient time,

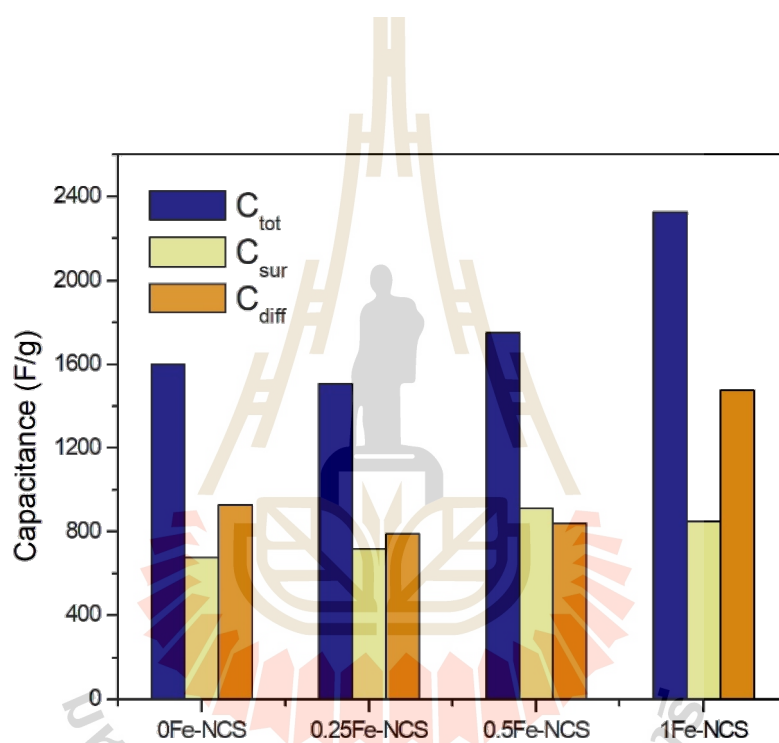
every reaction would occur even in the regions less accessible, the extrapolation of capacitance at 0 mV/s will provide the total capacitance ( $C_{\text{tot}}$ ). In contrast, the capacitance at very fast scan rate (infinity scan rate) is a result of only charges stored at the most accessible surface ( $C_{\text{sur}}$ ). Therefore,  $C_{\text{diff}}$  is the difference between  $C_{\text{tot}}$  and  $C_{\text{sur}}$ .



**Figure 4.18** (a) Capacitance *versus* the inverse of square root of scan rate and (b) Inverse capacitance *versus* the square root of scan rate.



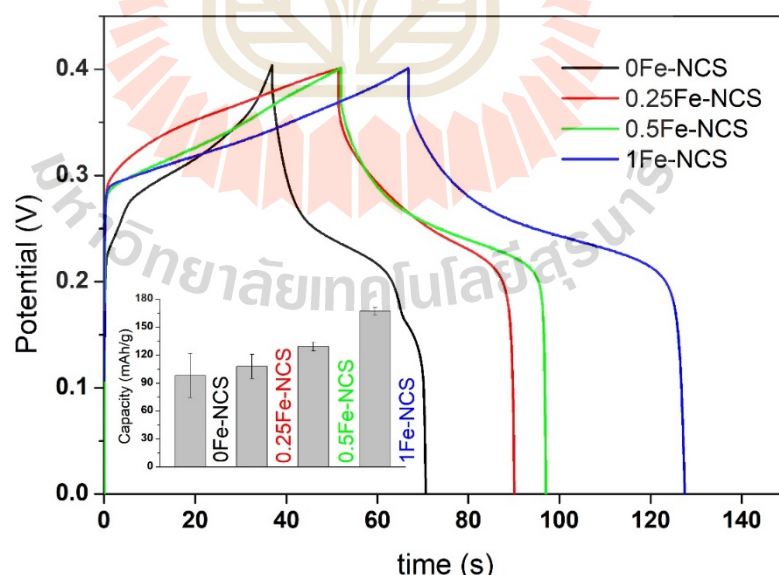
The obtained results are shown in Figure 4.19. Interestingly,  $C_{\text{sur}}$  do not significantly change with Fe content, implying that the surface areas of the samples are similar. Remarkably, the enhanced capacitance in 1Fe-NCS electrode come from the increase in  $C_{\text{diff}}$  which is capacitance contributed from diffusion-controlled process. Consequently, the higher  $C_{\text{diff}}$  in electrodes with high Fe content indicates that the diffusion of  $\text{OH}^-$  into inner surface of  $\text{NiCo}_2\text{S}_4$  materials is enhanced.



**Figure 4.19** The capacitance contributed from surface ( $C_{\text{sur}}$ ) and insertion process ( $C_{\text{diff}}$ ) derived from Trasatti's method.

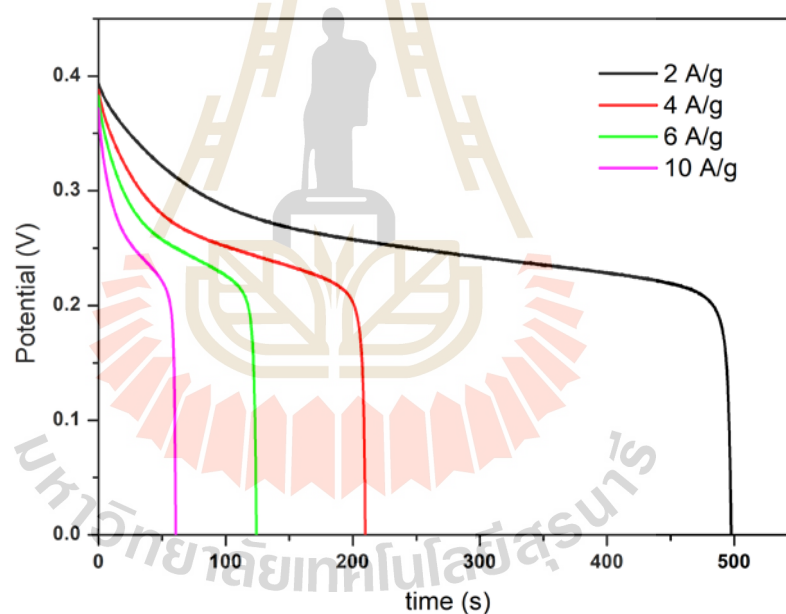
### 4.3.2 Galvanostatic charge-discharge (GCD)

Figure 4.20 shows Galvanostatic charge/discharge curves of all samples at the same current density of 10 A/g. As the amount of Fe addition increases, the discharge time also increases. We measured three electrodes in each condition and the average specific capacity with standard deviation as shown in the bar chart (Figure 4.20 inset) are  $98 \pm 23.5$ ,  $107.8 \pm 12.9$ ,  $129.1 \pm 4.8$  and  $167 \pm 4.1$  mAh/g for 0Fe-NCS, 0.25Fe-NCS, 0.5Fe-NCS and 1Fe-NCS, respectively. The 1Fe-NCS electrode shows the best electrochemical performance, with 1.7 times improvement from 0Fe-NCS. The capacity value of 1Fe-NCS is relatively high comparing to other NiCo<sub>2</sub>S<sub>4</sub>-based electrodes (Table 4.3). It is clear that, the specific capacity is increased with Fe-content in the samples. The enhanced capacity is caused by the change in the electrode's conductivity and morphology.



**Figure 4.20** Galvanostatic charge/discharge curves of all samples at current density of 10 A/g and the specific capacity of 0Fe-NCS, 0.25Fe-NCS, 0.5Fe-NCS and 1Fe-NCS electrodes (inset).

Figure 4.21 exhibits the galvanostatic discharge curves of the obtained 1Fe-NCS sample with potential window of 0 to 0.4 V at various current densities ranging from 2 to 10 A/g. It can be seen that along with increase in current densities, the discharge time decreases and the specific capacity of 1Fe-NCS electrode are 276.7, 233.4, 207.3 and 169.7 mAh/g at current density of 2, 4, 6 and 10 A/g, respectively. The decrease in capacity come from the inaccessibility of ions in some regions when increasing current density. At low current density, ions have enough time to penetrate into the inside of electrode material while at high current density, only the outer surface of electrode material can be utilized by ions during the charge-discharge process (Yang *et al.*, 2015).



**Figure 4.21** Galvanostatic discharge curves of 1Fe-NCS electrode at various current densities.

A plot of specific capacity as a function of current density for all samples are shown in Figure 4.22. The rate capabilities of 0Fe-NCS, 0.25Fe-NCS, 0.5Fe-NCS and 1Fe-NCS electrodes are 80%, 71%, 68% and 65%, respectively. Obviously, the 1Fe-NCS electrode exhibits the highest specific capacity among other electrodes at any

current densities. Although the rate capability of 1Fe-NCS is lower than the others, a high specific capacitance of 167 mAh/g is reached at a high current density of 10 A/g.

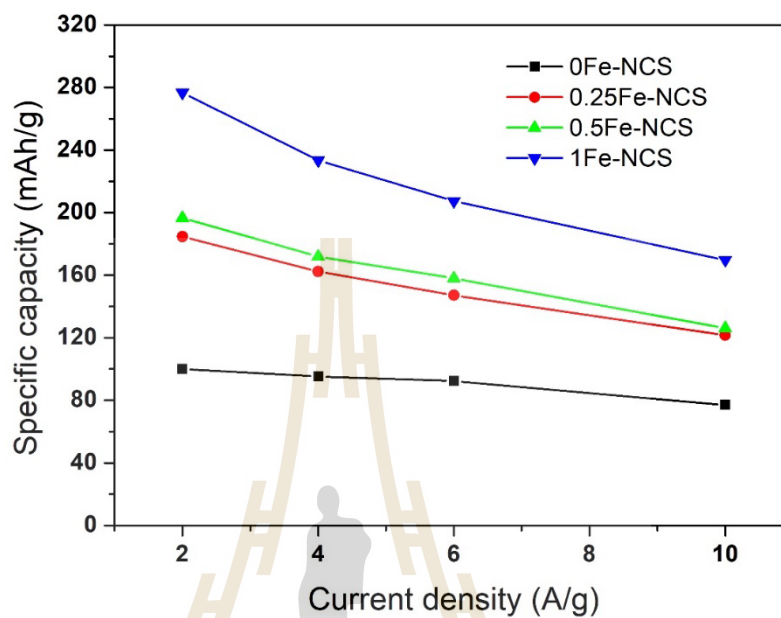


**Figure 4.22** Specific capacity as a function of current density for 0Fe-NCS, 0.25Fe-NCS, 0.5Fe-NCS and 1Fe-NCS electrodes.

**Table 4.3** NiCo<sub>2</sub>S<sub>4</sub> materials prepared by various methods and their performance.

<b>Materials</b>	<b>Synthetic technique</b>	<b>Specific capacity (mAh/g)</b>	<b>Ref.</b>
Nanosphere-like NiCo <sub>2</sub> S <sub>4</sub>	PVP-assisted hydrothermal method	70.6 at 4 A/g 77.6 at 2 A/g 82.6 at 1 A/g	Chen <i>et al.</i> , 2018
NiCo <sub>2</sub> S <sub>4</sub> arrays	hydrothermal	76.7 at 6 A/g 77.9 at 4 A/g 79.4 at 2 A/g 80.7 at 1 A/g	Wu <i>et al.</i> , 2019
NiCo <sub>2</sub> S <sub>4</sub> nanoflake	Electrodeposition using constant potential mode	154.4 at 4 A/g	Kumbhar <i>et al.</i> , 2019
NiCo <sub>2</sub> S <sub>4</sub> 3D honeycomb	Two-step hydrothermal	145.8 at 10 A/g 176.0 at 2 A/g	Shi <i>et al.</i> , 2019
Hierarchical NiCo <sub>2</sub> S <sub>4</sub> Core-Shell Nanowire Arrays	Two-step hydrothermal	228 at 10 A/g	Zou <i>et al.</i> , 2016

**Table 4.3** NiCo<sub>2</sub>S<sub>4</sub> materials prepared by various methods and their performance

(Continued).

Hierarchical porous NiCo <sub>2</sub> S <sub>4</sub> nanostructures	One-step hydrothermal	242 at 1 A/g	Wang <i>et al.</i> , 2016
MoS <sub>2</sub> /NiCo <sub>2</sub> S <sub>4</sub> @C hollow microspheres	Hydrothermal (self-template strategy)	238 at 10 A/g 250 at 2 A/g	Li <i>et al.</i> , 2020
NiCo <sub>2</sub> S <sub>4</sub> microaggregates	Two-step hydrothermal	167 at 10 A/g 238 at 2 A/g 249 at 1 A/g	Ren <i>et al.</i> , 2019
Fe-added NiCo <sub>2</sub> S <sub>4</sub>	One-step hydrothermal	169.7 at 10 A/g 207.3 at 6 A/g 233.4 at 4 A/g 276.7 at 2 A/g 351.1 at 1 A/g	This work

The cycling stability is an important factor for practical application evaluated by repeated charge-discharge measurements. The long cycle life is one of requirements for good supercapacitor electrodes. A plot of specific capacity as a function of cycle number at current density of 10 A/g is shown in Figure 4.23. The specific capacity slightly increases in the first 100 cycles, it is believed to cause by the activation of electrode materials (Pu *et al.*, 2014; Wang *et al.*, 2016; Zhang *et al.*, 2016). Then the specific capacity gradually decreases with increasing cycle numbers and 58% of their initial capacity can be retained after 1000 cycles. Li *et al.* reported that amorphous materials possess better cycle stability because amorphous structure can endure the structural changes during redox reaction (Li *et al.*, 2015). Therefore, the lower cycle stability in 1Fe-NCS sample can be explained by the increases in crystallinity.

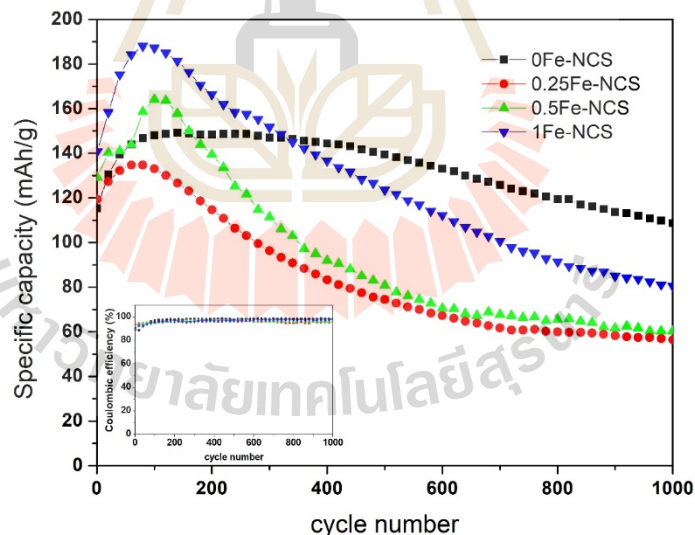


**Figure 4.23** cycle performance of all samples at current density of 10 A/g.

The SEM images of 0Fe-NCS and 1Fe-NCS electrodes before and after the cycling test are shown in Figure 4.24. Obviously, the electrode morphology of 1Fe-NCS was damaged after repeated charging/discharging 1000 cycles.

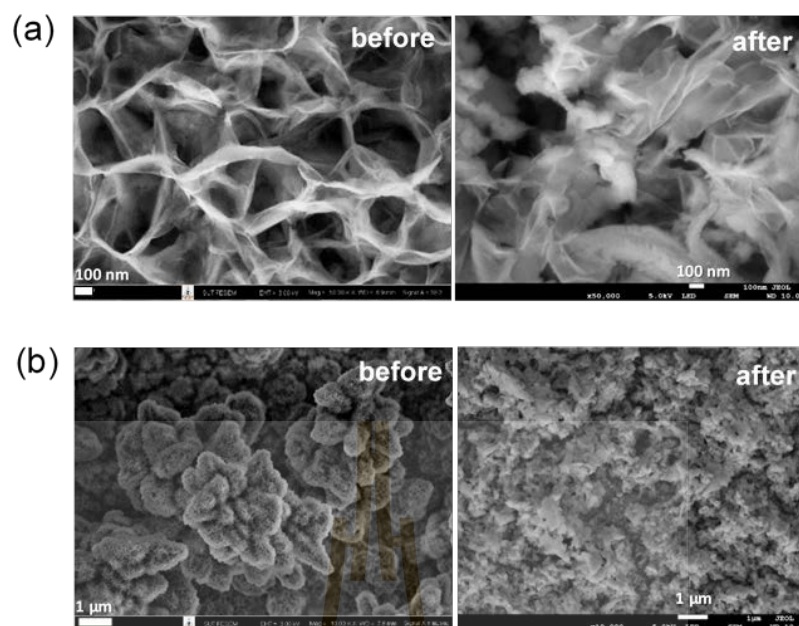


**Figure 4.24** SEM images of (a) 0Fe-NCS and (b) 1Fe-NCS before and after 1,000 cycles

The Coulombic efficiency ( $\eta$ ) during the cycling performance was determined by dividing discharging time with charging time. As shown in Figure 4.23 (inset), the Coulombic efficiencies of all samples remain at  $\sim 96\%$ , suggesting that the redox reactions of the electrodes are highly reversible (Wan *et al.*, 2013; Xiao *et al.*, 2015).

### 4.3.3 Electrochemical impedance spectroscopy (EIS)

The electrical conductivity of electrodes can be revealed by EIS measurements. Figure 4.25 shows EIS Nyquist plots of all samples. In general, this plot consists of a semicircle and a straight line. At high frequency, the intercept at real axis demonstrates an internal resistance ( $R_s$ ) and the diameter of semicircle represent the charge transfer resistance ( $R_{ct}$ ). The linear part at low frequency exhibits diffusive resistance (Walberg



impedance), indicating the diffusion rate of electrolyte ions. The straight line should be perpendicular to real axis for ideal supercapacitors (Li *et al.*, 2015).

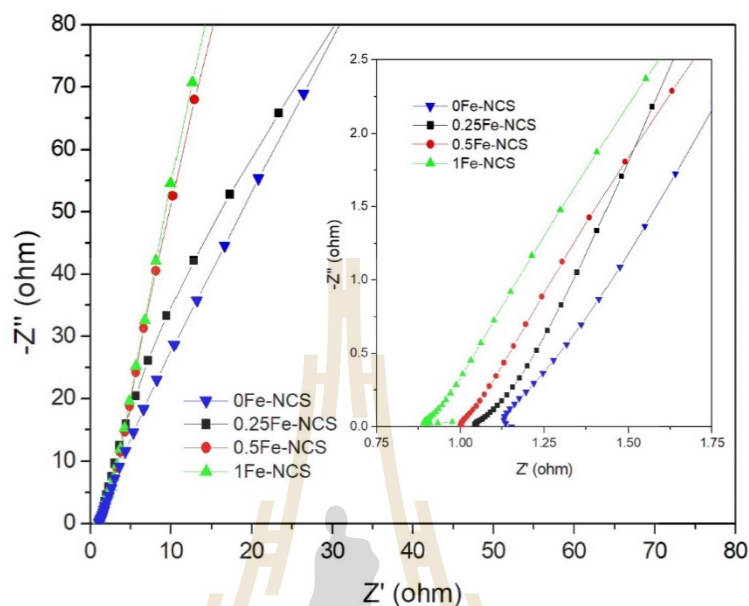


**Figure 4.25** EIS Nyquist plots of all samples (inset) the enlarge EIS Nyquist plots.

From EIS data, all samples display the small  $R_s$  and the small semicircles in high frequency region, indicating the low internal resistance and charge-transfer resistances during electrochemical processes (Lu *et al.*, 2016; Zhang *et al.*, 2017; Huo *et al.*, 2014). The low resistances are expected due to the metallic conducting behavior of  $\text{NiCo}_2\text{S}_4$  (Xia *et al.*, 2015). The 1Fe-NCS electrode possesses the lowest internal resistance and largest slope in the linear part which indicates the improvement in electrical conductivity of materials when Fe were added. The electrical conductivity is in the order of  $1\text{Fe-NCS} > 0.5\text{Fe-NCS} > 0.25\text{Fe-NCS} > 0\text{Fe-NCS}$  which is well consistent with the capacity trend. Therefore, the improved conductivity is one of the reasons for enhanced capacitive performance (Zhang *et al.*, 2017; Lu *et al.*, 2016; Ren *et al.*, 2019).

#### 4.4 Calculations

The effect of Fe doping on the electronic structures of  $\text{NiCo}_2\text{S}_4$  was investigated by projected density of states (PDOS). To do this, Co or Ni atom was substituted by one Fe atom in the  $\text{NiCo}_2\text{S}_4$  unit cell for doped systems. As shown in Figure 4.26, the calculated PDOS of the pristine and doped systems reveal that their Fermi energies lie within the band, demonstrating their metallic properties. Replacing Fe at the Co site results in higher DOS near the Fermi level which could enhance electronic conductivity of  $\text{NiCo}_2\text{S}_4$ . The calculated results are consistent with our current experiment based on the EIS results and previous computational works (Lai *et al.*, 2019). However, our dilute doping concentration shows only a small increase in DOS. For Fe doping at the Ni site, the DOS at the Fermi level is decreased suggesting a decrease in conductivity. Both experimental and computational results confirm that Fe doping improves electrical conductivity of  $\text{NiCo}_2\text{S}_4$ .

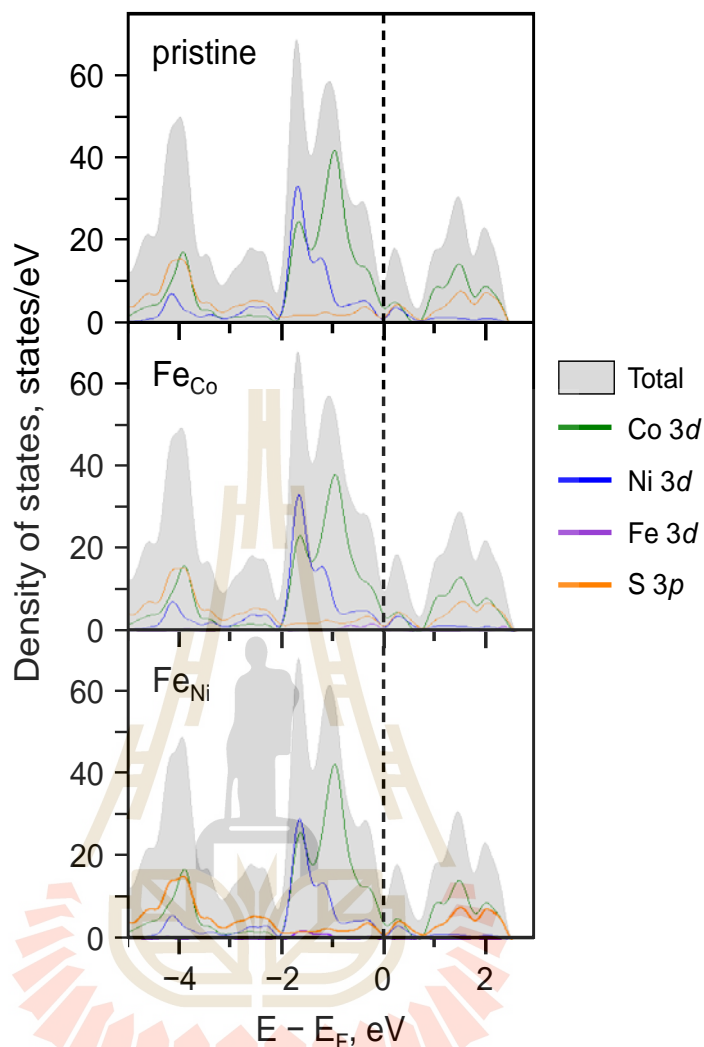


**Figure 4.26** PDOS of pristine, Fe-doped  $\text{NiCo}_2\text{S}_4$  bulk with doping sites at Co and Ni.

Furthermore, the electronic structures of electrode surfaces were analyzed to investigate the influence of Fe doping on the charge storage mechanism. To do this, a slab model of  $\text{NiCo}_2\text{S}_4$  (100) surface was created. The Fe-doped surfaces were obtained by replacing one transition metal (TM) atom with one Fe atom. We considered three different doping sites including Co and Ni sites on the topmost surface and a Ni site at the subsurface as schematically depicted in Figure 3.2 panel b and c. The computed

Bader charges (Figure 4.27) reveal that Fe doping at a Co site increases the electron densities of the neighboring S atoms and S atoms have more negative net charges. On the other hand, Fe doping at Ni sites either on the topmost or subsurface layer does not display charge accumulation at the neighboring S atoms. In addition, the calculated PDOS of the surfaces (Figure 4.28) show that the d-band center shifts closer to the Fermi level from  $-1.30$  eV to  $-1.26$  eV when Fe replaces Co, suggesting the higher chemical adsorption capability. In contrast, d-band centers of Fe doping at Ni sites shift toward the negative energy from  $-1.30$  eV to  $-1.34$  eV, indicating the weaker adsorption ability.

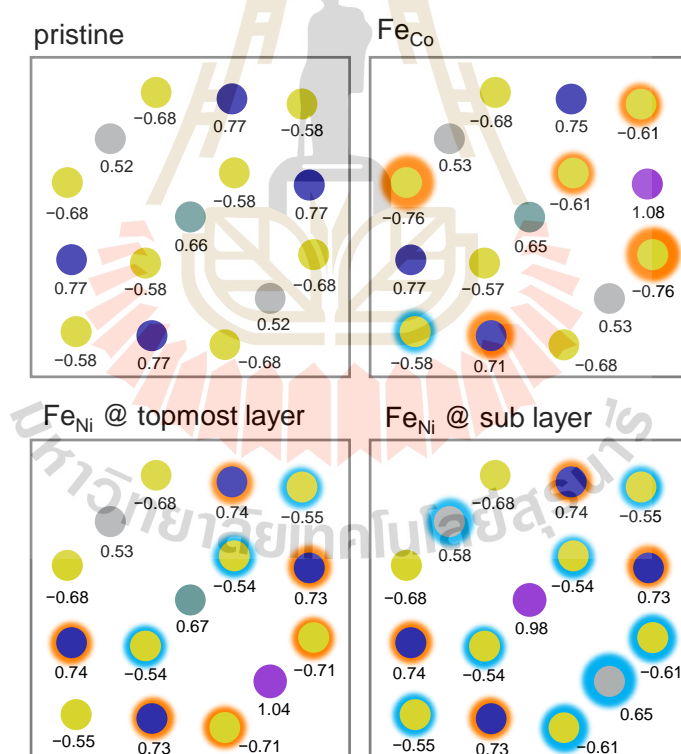


**Figure 4.27** Bader charges of the two topmost layers of pristine and Fe-doped surfaces where grey, teal, dark blue, and yellow circles represent Ni at topmost layer, Ni at subsurface layer, Co, and S atoms, respectively. The light blue and orange shadow highlight the negative and positive changes of charges upon doping.

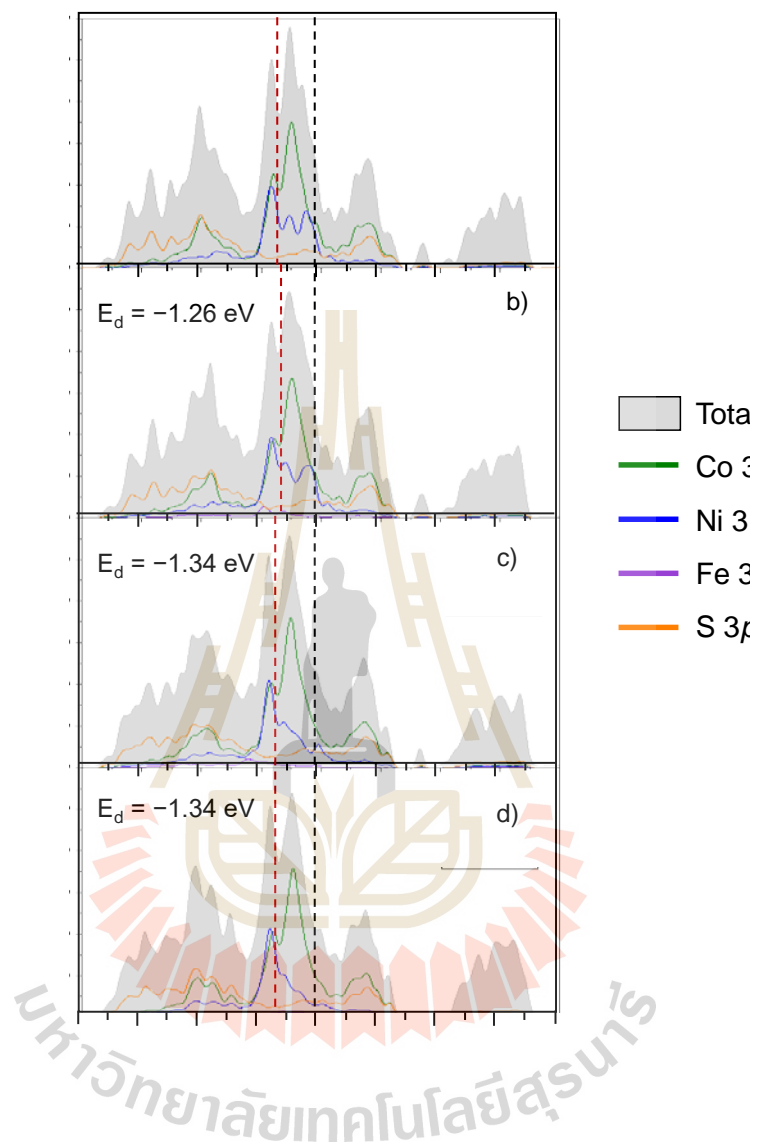


**Figure 4.28** Projected density of states (PDOS) of a) pristine, b) Fe substitution at Co, c) Fe substitution at topmost-layered Ni, and d) Fe substitution at sub-layered Ni of  $\text{NiCo}_2\text{S}_4$  (100) surfaces. The calculated values of d-band center,  $E_d$ , are indicated in the inset

Since the redox reactions of  $\text{NiCo}_2\text{S}_4$  in the electrolyte (equation 9-11) require both active species to react with  $\text{OH}^-$ , the electrolyte-electrode interactions play a key role in evaluating their electrochemical properties. Thus, we further studied the formation of KOH electrical double layer (EDL) at the electrode interface. In the surface model, there are six TM sites on the topmost layer. Six formula units of KOH were added on the surface where  $\text{OH}^-$  ions were placed on the atop sites of TM atoms. In the second layer next to the  $\text{OH}^-$  ions, the  $\text{K}^+$  counter ions were added to model the electrical double layer formed during the charge storage. The equilibrium structures of KOH electrolyte on the surfaces is obtained by relaxation of internal coordinates. As shown in Figure 4.29, four  $\text{OH}^-$  ions chemically adsorb on the surface and form TM–O bonds while the other two  $\text{OH}^-$  ions weakly adsorb on the S sites pointing their H ends toward the surface.

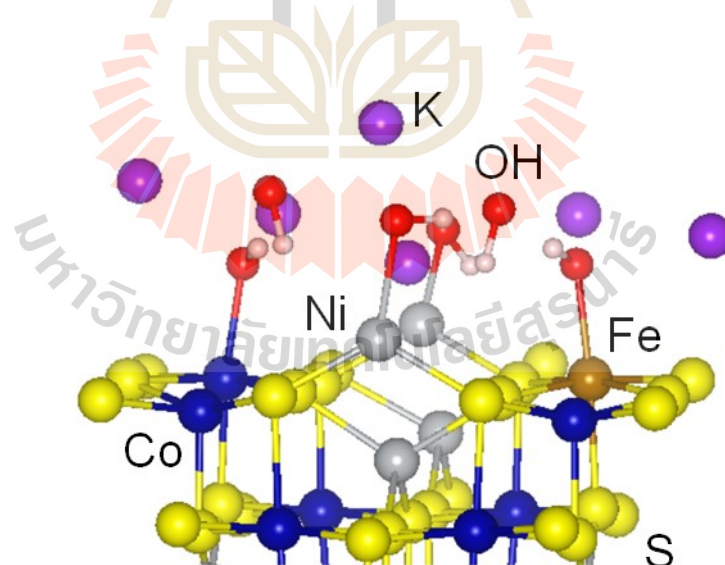


**Figure 4.29** Formation of KOH electrical double layer on the Fe-doped surface at a Co site.

The calculated adsorption energies of Fe doping at the Co site is lower than that of the pristine surface ( $-2.24$  vs  $-2.07$  eV / KOH), indicating that the electrolyte interaction is improved. On the contrary, doping at Ni sites show higher energy ( $-1.99$  and  $-1.92$  eV / KOH) suggesting that the stability of KOH on the electrode surfaces is slightly lower. The calculated adsorption energies are in agreement with the electronic structure calculations. Only the Fe replaced Co surface enhances adsorptivity of KOH electrolyte on the surface. Based on the experimental and calculational results, it is therefore more likely that Fe in the samples are replacing Co rather than Ni. The improved EDL-surface interaction suggests that replacing Co with Fe facilitates the  $\text{OH}^-$  adsorption which improves the reactivity of both metallic ions to react with  $\text{OH}^-$  resulting in increasing electrode performance.

#### 4.5 References

- Ardizzone, S., Fregonara, G., and Trasatti, S. (1990) "Inner" and "outer" active surface of  $\text{RuO}_2$  electrodes. **Electrochimica Acta**. 35: 263-267.
- Bonnin-Mosbah, M., Metrich, N., Susini, J., Salome, M., Massare, D., and Menez, B. (2002) Micro X-ray absorption near edge structure at the sulfur and iron K-edges in natural silicate glasses. **Spectrochimica Acta Part B**. 57: 711-725.
- Chen, X., Chen, D., Guo, X., Wang, R., and Zhang, H. (2017) Facile Growth of Caterpillar-like  $\text{NiCo}_2\text{S}_4$  Nanocrystal Arrays on Nickle Foam for High-Performance Supercapacitors. **ACS Applied Materials & Interfaces**. 9(22): 18774-18781.

- Chen, Y. Y., Dhaiveegan, P., Michalska, M., and Lin, Y. L. (2018) Morphology-controlled synthesis of nanosphere-like  $\text{NiCo}_2\text{S}_4$  as cathode materials for high-rate asymmetric supercapacitors. **Electrochimica Acta**. 274: 208-216.
- Duay, J., Sherrill, S. A., Gui, Z., Gillette, E., and Lee, S. B. (2013) Self-limiting electrodeposition of hierarchical  $\text{MnO}_2$  and  $\text{M(OH)}_2/\text{MnO}_2$  nanofibril/nanowires: Mechanism and supercapacitor properties. **ACS Nano**. 2: 1200-1214.
- Huang, Y., Shi, T., Jiang, S., Cheng, S., Tao, X., Zhong, Y., Liao, G., and Tang, Z. (2016) Enhanced cycle stability of  $\text{NiCo}_2\text{S}_4@/\text{NiO}$  core-shell nanowire arrays for all-solid-state asymmetric supercapacitors. **Scientific Reports**. 6: 38620.
- Huo, H., Zhao, Z., and Xu, C. (2014) 3D  $\text{Ni}_3\text{S}_2$  nanosheet arrays supported on Ni foam for high-performance supercapacitor and non-enzymatic glucose detection. **Journal of Materials Chemistry A**. 2: 15111-15117.
- Jinlong, L., Tongxiang, L., Meng, Y., Suzuki, K., and Miura, H. (2017) The plume-like  $\text{Ni}_3\text{S}_2$  supercapacitor electrodes formed on nickel foam by catalysis of thermal reduced graphene oxide. **Journal of Electroanalytical Chemistry**. 786: 8-13.
- Kornienko, N., Resasco, J., Becknell, N., Jiang, C. M., Liu, Y. S., Nie, K., Sun, X., Guo, J., Leone, S. R., and Yang, P. (2015) *Operando* Spectroscopic Analysis of an Amorphous Cobalt Sulfide Hydrogen Evolution Electrocatalyst. **Journal of the American Chemical Society**. 137: 7448-7455.
- Krishnamoorthy, K., Veerasubramani, G. K., Radhakrishnan, S., and Kim, S. J. (2014) One pot hydrothermal growth of hierarchical nanostructured  $\text{Ni}_3\text{S}_2$  on Ni foam for supercapacitor application. **Chemical Engineering Journal**. 251: 116-122.



- Kumbhar, V. S., Chodankar, N. R., Lee, K., and Kim, D-H. (2019) Insights into the interfacial nanostructuring of  $\text{NiCo}_2\text{S}_4$  and their electrochemical activity for ultra-high capacity all-solid-state flexible asymmetric supercapacitors. **Journal of Colloid and Interface Science**. 557: 423-437.
- Lai, F., Feng, J., Heil, T., Tian, Z., Schmidt, J., Wang, G. C., and Oschatz, M. (2019) Partially delocalized charge in Fe-doped  $\text{NiCo}_2\text{S}_4$  nanosheet-mesoporous carbon-composites for high-voltage supercapacitors. **Journal of Materials Chemistry A**. 7: 19342-19347.
- Latif, C., Negara, V. S. I., Wongtepa, W., Thamatkeng, P., Zainuri, M., and Pratapa, S. (2018) Fe K-Edge X-ray absorption near-edge spectroscopy (XANES) and X-ray diffraction (XRD) analyses of  $\text{LiFePO}_4$  and its base materials. **Journal of Physics: Conference Series**. 985.
- Li, Q., Lu, W., Li, Z., Ning, J., Zhong, Y., and Hu, Y. (2020) Hierarchical  $\text{MoS}_2/\text{NiCo}_2\text{S}_4@\text{C}$  urchin-like hollow microspheres for asymmetric supercapacitors. **Chemical Engineering Journal**. 380: 122544.
- Li, X., Jiang, L., Zhou, C., Liu, J., and Zeng, H. (2015) Integrating large specific surface area and high conductivity in hydrogenated  $\text{NiCo}_2\text{O}_4$  double-shell hollow spheres to improve supercapacitors. **NPG Asia Materials**. 7: 1-7.
- Li, X., Li, Q., Wu, Y., Rui, M., and Zeng, H. (2015) Two-Dimensional, Porous Nickel-Cobalt Sulfide for High-performance asymmetric supercapacitors. **ACS applied Materials & Interfaces**. 7: 19316-19323.
- Lin, L., Liu, J., Liu, T., Hao, J., Ji, K., Sun, R., Zeng, W., and Wang, Z. (2015) Growth-controlled  $\text{NiCo}_2\text{S}_4$  nanosheet arrays with self-decorated nanoneedles for high-

- performance pseudocapacitors. **Journal of Materials Chemistry A**. 3: 17652-17658.
- Liu, X. and Wu, Z. (2017) Hierarchitectures of mesoporous flowerlike NiCo<sub>2</sub>S<sub>4</sub> with excellent pseudocapacitive properties. **Materials Letters**. 187: 24-27.
- Lu, F., Zhou, M., Li, C., Xue, Y., Jiang, X., Zeng, X., Bando, Y., and Golberg, D. (2016) Engineering sulfur vacancies and impurities in NiCo<sub>2</sub>S<sub>4</sub> nanostructures toward optimal supercapacitive performance. **Nano Energy**. 26: 313-323.
- Moulder, J. F., Stickle, W. F., Sobol, P. E., and Bomben, K. D. (1992) Handbook of X-ray Photoelectron Spectroscopy: A Reference Book of Standard Spectra for Identification and Interpretation of XPS data. **Perkin-Elmer Corporation**. Physical Electronics Division.
- Peng, S., Li, L., Li, C., Tan, H., Cai, R., Yu, H., Mhaisalkar, S., Srinivasan, M., Ramakrishna, S., and Yan, Q. (2013) In situ growth of NiCo<sub>2</sub>S<sub>4</sub> nanosheets on graphene for high-performance supercapacitors. **Chemical Communications**. 49: 10178-10180.
- Phokha, S., Klinkaewnarong, J., Hunpratub, S., Boonserm, K., Swatsitang, E., and Maensiri, S. (2016) Ferromagnetism in Fe-doped MgO nanoparticles. **Journal of Materials Science: Material in electronics**. 27:33-39.
- Pu, J., Wang, T., Wang, H., Tong, Y., Lu, C. Kong, W., and Wang, Z. (2014) Direct Growth of NiCo<sub>2</sub>S<sub>4</sub> Nanotube Arrays on Nickel Foam as High-Performance Binder-Free Electrodes for Supercapacitors. **ChemPlusChem**. 79: 577-583.
- Ren, X., Du, Y., Song, M., Chen, Y., Zhou, Y., Ma, F., and Wan, J. (2019) Facile preparation of mesoporous NiCo<sub>2</sub>S<sub>4</sub> microaggregates constructed by

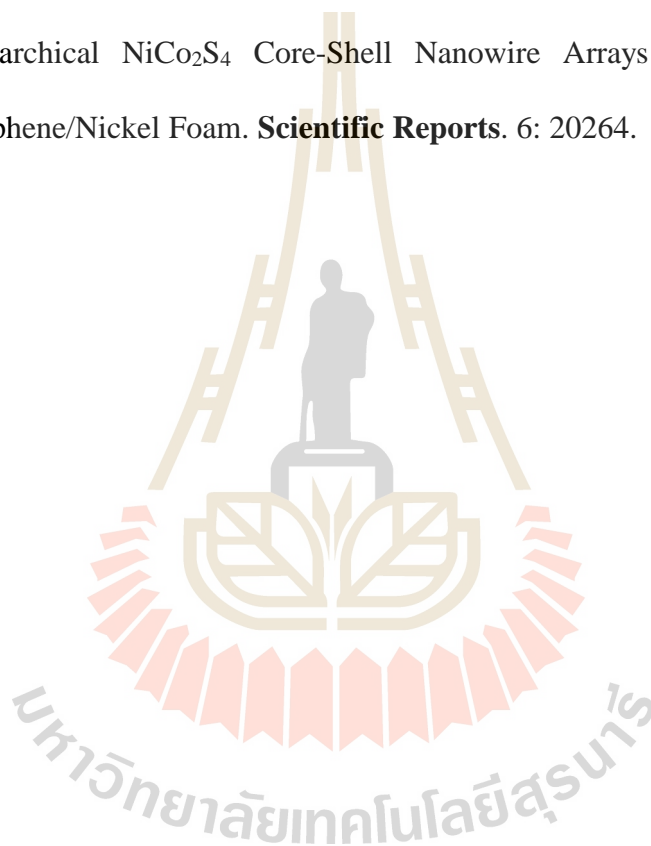
- nanoparticles via puffing  $\text{NiCo}_2\text{O}_4$  cubes for high performance asymmetric supercapacitors. **Journal of Alloys and Compounds**. 806: 1481-1490.
- Shao, J. Zhou, X., Liu, Q., Zou, R., Li, W., Yang, J., and Hu, J. (2015) Mechanism analysis of the capacitance contributions and ultralong cycling-stability of the isomorphous  $\text{MnO}_2@\text{MnO}_2$  core/shell nanostructures for supercapacitors. **Journal of Materials Chemistry A**. 3: 6168-6176.
- Shen, L., Yu, L., Wu, H. B., Yu, X. Y., Zhang, X., and Lou, X. W. (2015) Formation of nickel cobalt sulfide ball-in-ball hollow spheres with enhanced electrochemical pseudocapacitive properties. **Nature Communications**. 6: 6694.
- Shi, B., Saravanakumar, B., Wei, W., Dong, G., Wu, S., Lu, X., Zeng, M., Gao, X., Wang, Q., Zhou, G., Liu, J-M., Kempa, K., and Gao, J. (2019) 3D honeycomb  $\text{NiCo}_2\text{S}_4 @ \text{Ni}(\text{OH})_2$  nanosheets for flexible all-solid-state asymmetric supercapacitors with enhanced specific capacitance. **Journal of Alloys and Compounds**. 790: 693-702.
- Wan, H., Jiang, J., Yu, J., Xu, K., Miao, L., Zhang, L., Chen, H., and Ruan, Y. (2013)  $\text{NiCo}_2\text{S}_4$  porous nanotubes synthesis via sacrificial templates: high-performance electrode materials of supercapacitors. **CrystEngComm**. 15: 7649-7651.
- Wang, J. G., Zhou, R., Jin, D., Xie, K., and Wei, B. (2016) Controlled synthesis of  $\text{NiCo}_2\text{S}_4$  nanostructures on nickel foams for high-performance supercapacitors. **Energy Storage Materials**. 2: 1-7.

- Wang, J. G., Jin, D., Zhou, R., Shen, C., Xie, K., and Wei, B. (2016) One-step synthesis of  $\text{NiCo}_2\text{S}_4$  ultrathin nanosheets on conductive substrates as advanced electrodes for high-efficient energy storage. **Journal of Power Sources**. 306: 100-106.
- Wei, C., Huang, Y., Xue, S., Zhang, X., Chen, X., Yan, J., and Yao, W. (2017) One-step hydrothermal synthesis of flaky attached hollow-sphere structure  $\text{NiCo}_2\text{S}_4$  for electrochemical capacitor application. **Chemical Engineering Journal**. 317: 873-881.
- Wu, J., Huang, X., and Xia, X. (2019) Exploring  $\text{NiCo}_2\text{S}_4$  nanosheets arrays by hydrothermal conversion for enhanced high-rate batteries. **Journal of Energy Chemistry**. 35: 132-137.
- Xia, C., Li, P., Gandi, A. N., Schwingenschlogl, U., and Alshareef, H. N. (2015) Is  $\text{NiCo}_2\text{S}_4$  really a semiconductor?. **Chemistry of Materials**. 27: 6482-6485.
- Xiao, Y., Lei, Y., Zheng, B., Gu, L., Wang, Y., and Xiao, D. (2015) Rapid microwave-assisted fabrication of 3D cauliflower-like  $\text{NiCo}_2\text{S}_4$  architectures for asymmetric supercapacitors. **RSC Advance**. 5: 21604-21613.
- Yang, Z., Zhu, X., Wang, K., Ma, G., Cheng, H., and Xu, F. (2015) Preparation of  $\text{NiCo}_2\text{S}_4$  flaky arrays on Ni foam as binder-free supercapacitor electrode. **Applied Surface Science**. 347: 690-695.
- Yuan, Y., Long, D., Li, Z., and Zhu, J. (2019) Fe substitution in urchin-like  $\text{NiCo}_2\text{O}_4$  for energy storage devices. **RSC Advance**. 9: 7210-7217.
- Zhang, Z., Huang, X., Li, H., Zhao, Y., and Ma, T. (2017) 3-D honeycomb  $\text{NiCo}_2\text{S}_4$  with high electrochemical performance used for supercapacitor electrodes. **Applied Surface Science**. 400: 238-244.

Zhou, H., Zou, X., Zhang, K., Sun, P., Islam, M. S., Gong, J., Zhang, Y., and Yang, J.

(2017) Molybdenum–Tungsten Mixed Oxide Deposited into Titanium Dioxide Nanotube Arrays for Ultrahigh Rate Supercapacitors. **ACS Applied Materials & Interfaces**. 9 (22): 18699-18709.

Zou, R., Yuen, M. F., Yu, L., Hu, J., Lee, C-S., and Zhang, W. (2016) Electrochemical Energy Storage Application and Degradation Analysis of Carbon-Coated Hierarchical NiCo<sub>2</sub>S<sub>4</sub> Core-Shell Nanowire Arrays Grown Directly on Graphene/Nickel Foam. **Scientific Reports**. 6: 20264.



## CHAPTER V

### CONCLUSION

We have successfully synthesized a series of Fe-added NiCo<sub>2</sub>S<sub>4</sub>, directly grown on Ni foam via a simple one-step hydrothermal method. The performance of Fe-added NiCo<sub>2</sub>S<sub>4</sub> binder-free electrodes can be improved by increasing the amount of FeCl<sub>3</sub>. Here, FeCl<sub>3</sub> additive plays two different roles in the synthesis. It promotes a 3D growth of highly crystalline materials in hydrothermal reaction and serves as a source providing Fe<sup>3+</sup> to NiCo<sub>2</sub>S<sub>4</sub> lattice. The changes in both the morphology and the lattice result in an improved electrical conductivity and enhanced ion diffusion. The 1Fe-NCS electrode exhibits the highest specific capacitance of 167 mAh/g at a current density of 10 A/g, 1.7 times that of the undoped NiCo<sub>2</sub>S<sub>4</sub> electrode. The obtained electrodes exhibit good rate capability and moderate cycle stability. These results suggest that metallic doping can be an interesting strategy to improve the performance of NiCo<sub>2</sub>S<sub>4</sub>-based electrodes for supercapacitor applications.

## CURRICULUM VITAE

**Name** Miss Praphaiphon Phonsuksawang

**Address** 190-192 Chompol road, Naimuang Sub-District, Muang District,  
Nakhon Ratchasima Province, Thailand, 30000

**Education**

2013-2016 B.Sc. First Class Honors (Chemistry), Suranaree University of  
Technology, Thailand

2017-2020 Student at school of chemistry, Suranaree University of Technology,  
Thailand

**Scholarship**

2013-2020 Thai government, “Development and Promotion of Science and  
Technology Talent Project, DPST”

**Publication**

**Phonsuksawang, P.,** Khajondetchairit, P., Butburee, T., Sattayaporn, S., Chanlek, N.,  
Hirunsit, P., Suthirakun, S., Siritanon, T. (2020). Effects of Fe doping on enhancing  
electrochemical properties of NiCo<sub>2</sub>S<sub>4</sub> supercapacitor electrode. **Electrochimica Acta.**  
340: 135939.